Multi-scale Interaction between a Tearing Mode and a Collisional Drift Wave

Hayashi, Takayuki
Interdisciplinary Graduate School of Engineering Sciences, Kyushu University

Ito, Sanae-I.
Research Institute for Applied Mechanics, Kyushu University

Yagi, Masatoshi
Research Institute for Applied Mechanics, Kyushu University

Azumi, Masafumi
Center for Computational Science and Systems, Japan Atomic Energy Agency

https://doi.org/10.15017/26831

出版情報：九州大学応用力学研究所所報. 133, pp.19-39, 2007-09. Research Institute for Applied Mechanics, Kyushu University

Multi-scale Interaction between a Tearing Mode and a Collisional Drift Wave

Takayuki HAYASHI, *1Sanae-I. ITOH*2, Masatoshi YAGI*2
and Masafumi AZUMI *3

E-mail of corresponding author: *takayuki@riam.kyushu-u.ac.jp*

(Received April 10, 2007)

Abstract

The interaction between tearing mode and collisional drift wave is investigated using reduced neoclassical MHD equations. Introducing two types of neoclassical viscosity model, i.e., HS model and B model, the stability analysis of tearing mode and collisional drift wave is performed. It is found that both (neoclassical) tearing mode and collisional drift wave are unstable for B model even in the optimized q profile with $\Delta' = 0$. Next, the nonlinear simulation in case with B model is performed. It is found that the growth rate of tearing mode is enhanced by the beat interaction of collisional drift wave.

Key words : *magnetic island, tearing mode, MHD, high β, ITER, NTM, instability, simulation*

1. Introduction

The tearing mode is an important resistive magnetohydrodynamics (MHD) mode [1]. It perturbs the initial equilibrium magnetic flux surface through magnetic field reconnection to form new flux surfaces with magnetic islands. Nonlinear theory for the tearing mode began in 1973 when Rutherford showed that the mode ceases exponential growth and enters a domain of algebraic growth as soon as the island is larger than the tearing layer [2]. This slowing down of the mode is due to the formation of an inductive current flowing at the island O-point, parallel to the Ohmic current. The evolution of the magnetic island in the tearing mode to a saturated state could be predicted by a generation of Δ' to the case of finite island width, i.e., that the island state simply found a width determined by a magnetic energy minimum and then only slowly changed its width to follow the slower resistive evolution of the current profile [3]. This allows for the possibility of stable configurations which possess magnetic islands and exhibit Mirnov oscillations.

The magnetic islands are often observed in tokamak plasmas with high plasma β (the ratio of plasma pressure to magnetic pressure) even in the case that classical tearing modes are stable [4, 5]. The neoclassical bootstrap current is considered as a plausible candidate to drive these magnetic islands in a high β plasma, so that this nonlinear instability is called the Neoclassical Tearing Mode (NTM). Since magnetic islands deteriorate the plasma confinement, it is important to understand the trigger condition for its onset and the detailed physical mechanism of NTM, in order to attain the self-ignition condition in ITER (International Thermonuclear Experimental Reactor).

Much work on NTM has been done [6, 7] and it is found that the predicted width of saturated island, determined by the balance between the fluctuating bootstrap current and the current of free energy source, is considered to be consistent with experimental observations. However, the trigger condition or the dynamics are still unclear from the view point of the conventional approach.

In theoretical studies carried out so far, the linear analysis of NTM is performed using a three-field model and is compared with the one by four-field model which includes ion neoclassical viscosity and compressibility [8]. It is found that both the parallel compressibility and the ion neoclassical viscosity stabilize NTM. Later, the modified Rutherford equation has been derived based on the four-field model using the conventional ordering scheme [9]. However, it is shown that this model contains a serious problem, i.e., no stable stationary solution is found. This may be related with the assumption of the ordering scheme, however, no an-

*1 Interdisciplinary Graduate School of Engineering Sciences, Kyushu University
*2 Research Institute for Applied Mechanics, Kyushu University
*3 Center for Computational Science and Systems, Japan Atomic Energy Agency

alytical solution is obtained even if a more general ordering is adopted. Therefore, in order to understand the characteristics of solution, the direct simulation using four-field model is desired to investigate the island evolution. In addition, there is another problem for the model equation which describes the NTM. In the past analysis, the Hirshman-Sigmar viscosity model was been used, however, neoclassical viscosity is derived based on neoclassical ordering which might be irrelevant for drift wave time scale. For ever the conventional NTM model, the nonlinear simulation is very difficult for fusion relevant parameter regime, therefore, some simplification is necessary. So far, we can not resolve this contradiction, so that we use both Hirshman-Sigmar model and the simplified model which we call as banana viscosity model in this thesis.

In this thesis, nonlinear simulation of NTM based on four-field reduced neoclassical magnetrohydrodynamics (MHD) model is performed and the nonlinear acceleration and saturation mechanism of NTM are investigated.

The organization of this thesis is as follows : In Chapter 2, we review collapse phenomena in high temperature tokamak plasma such as a sawtooth oscillation and a tearing mode. Theoretical approaches based on linear and nonlinear theory of tearing modes are also explained. Viscosities in the three types of collisional regime are guided. In Chapter 3, model equations and initial profiles are explained. In Chapter 4, simulation results are discussed. Finally, Summary is given in Chapter 5.

2. Reviews

For an achievement of self-ignited plasma, it is important to investigate the mechanism of crash and collapse phenomena in high temperature plasma and control them. There are various types of such events in troidal plasmas. The references on the physics of collapses are found in the review paper [12]. Fig. (1) shows the characteristics of crash events, precursors and triggering mode.

In this chapter, examples of such collapse events are reviewed.

2.1 Trigger Events

The trigger phenomena have been very widely observed under various types of plasma confinement properties. Especially, $m/n = 1/1$ mode shown in Fig. (1) leads to various trigger mode or precursor mode, so it is a key to understanding collapse and the disruption(thermal quench). Sawtooth, disruption, high β collapse are the typical examples. However, we should distinguish them from the view point of physical mechanisms even though they have the same poloidal/troidal mode numbers.

Name	Observed response	Time scale	Trigger mode	Precursor mode	Note
Sawtooth	$T_e n_e$ $\Delta q \sim 0.05$	$< 100\ \mu s$	$m/n = 1/1$ etc (?)	$m/n = 1/1$	No full-reconnection $q(0) < 1$
Partial sawtooth	As above	←	←	←	←
Disruption (thermal quench)	T_e	10–$100\ \mu s$	$m/n = 1/1$ 'erosion'	$m/n = 2/1$ 3/1 etc	Density limit, $q = 2, 3$
High-β collapse (tokamak)	T_e (T_i)	$< 100\ \mu s$	$n \gg 1$ ballooning	$m/n = 1/1$ etc	$\beta \sim \beta_c^{\mathrm{MHD}}$
Internal collapse (Heliotron)	T_e	$< 100\ \mu s$	$m/n = 2/1$ interchange	$m/n = 2/1$	
ELMs (type-I)	$T_e T_i n_e$	10–$100\ \mu s$	$n \gg 1$	—	$\alpha \sim \alpha_c^{\mathrm{MHD}}$
X-event	$\chi_i T_i$	$< 100\ \mu s$	—	—	High-T_i mode
BLM	∇T_e	$< 100\ \mu s$	$m/n = 3/1$ Infernal?	—	High-β_p mode
MTE	∇V_φ	$< 100\ \mu s$	$n \gg 1$	—	Prohibits VH-mode
CHS burst	$\phi(r)$	few $100\ \mu s$	$m/n = 2/2$	$m/n = 2/1$	NBI injection
IRE	t_i				Low-aspect radio tokamak

Fig. 1 Crash events, precursors and triggering modes. Abbreviations: ELMs(edge-localized modes), MTE(momentum transfer events), BLM(barrier-localized mode), IRE(internal reconnection events) (quoted from [4]).

Sawtooth has been known as the process that a $m/n = 1/1$ perturbation occurs and it precedes the decay of the central electron temperature. This perturbation is called a precursor. The observation of the precursor stimulated the study of the m/n = 1/1 instabilities in tokamaks. Precise measurements of the development of the helical deformation have been made over the years. Figure (2) shows a typical example from the JET tokamak. Phenomena in Fig. (2) are widely observed on many tokamaks and considered to be universal. The helical shift of the peak of the soft X-ray emission intensity is plotted as a function of time. In the precursor phase, the helical shift is in the range of 1-3 cm and grows very slowly. The helical deformation, at some instant, abruptly starts to grow. If one plots the temporal evolution of the growth rate of the helical deformation, it suddenly changes in an unpredictable manner, a phase which is often called a "magnetic trigger".

2.2 Magnetic Island

The magnetic island is widely observed in high β tokamak plasmas. This structure is formed by the reconnection of the poloidal magnetic field line. Figure (3) shows the-dimensional structure of $m/n = 2/1$ magnetic island in a toroidal plasma. It locally flattens the

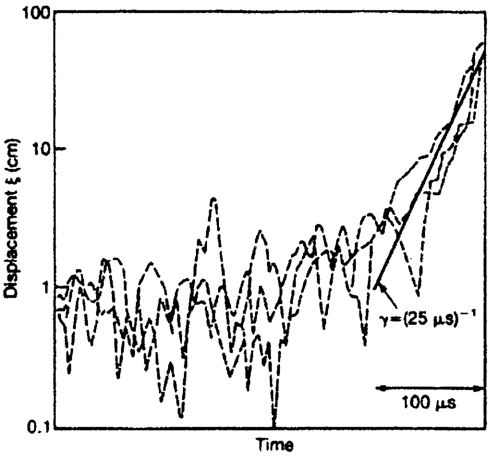

Fig. 2 Displacement of the sort X-ray emission peak during a fast sawtooth collapse observed on the JET tokamak (quoted from [15]).

plasma temperature and density profiles, thereby degrading the overall energy and particle confinement. In particular, the island width determines the level of the degradation of plasma confinement, therefore, it is important to clarify the mechanism of island saturation.

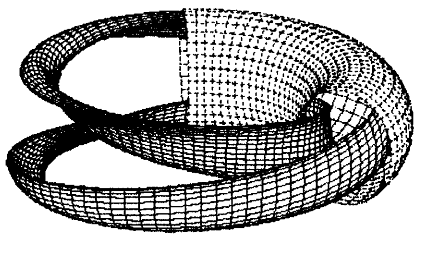

Fig. 3 The three-dimensional structure of the $m/n = 2/1$ island in toroidal plasma.

The analysis has been performed in a cylindrical geometry with the coordinates (r, θ, z) and the magnetic field of $\mathbf{B} = (0, B_\theta(r), B_z)$. Consider a saturated tearing instability with m periods in poloidal direction (θ) and n periods in the toroidal (z) direction. The perturbed poloidal flux ψ takes the general form

$$\psi(r, \theta, z, t) = \psi(r) \cos\zeta \tag{1}$$

Here, ζ is the helical phase angle of the mode, which is defined by $\zeta = m\theta - nz/R$.

According to ideal MHD, the magnetic perturbation obeys

$$\frac{1}{r}\frac{d}{dr}\left(r\frac{d\psi}{dr}\right) - \frac{m^2}{r^2}\psi - \frac{\mu_0 J_z'}{B_\theta(1 - \frac{q}{q_s})}\psi = 0 \tag{2}$$

where $q(r) = rB_z/RB_\theta(r)$ is the safety factor profile and $q_s \equiv q(r_s) = m/n$ defines the position of the "rational" flux surface. On the surface, lines of magnetic force close in finite number of rotation.

In the vicinity of the rational surface,

$$\psi(r) \simeq \Psi \tag{3}$$

for tearing instabilities, where Ψ implies a constant magnetic flux function and $\Psi > 0$ is termed "reconnected flux". Equation (2.3) is equivalent to the well-known "constant-ψ" approximation [10]. The growth rate of the resistive modes is determined by requiring that the discontinuity of the "inner" solution should match that of the "outer" solution. Then we need to calculate the change in logarithmic derivative $\Delta'_{int}(\gamma)$ of the "inner" solution across the resistive layer and the growth rate γ can be obtained from the eigenvalue equation

$$\Delta'_{int}(r) = \Delta' \tag{4}$$

Δ' indicates the discontinuity of the first derivative of perturbed field component across the rational surface given by

$$\Delta' = \frac{\psi'(0+) - \psi'(0-)}{\psi(0)} \tag{5}$$

For the nonlinear evolution of tearing mode, Rutherford theory has an important suggestion. When the magnetic island width exceeds the linear tearing layer width, the island dynamics becomes strongly nonlinear and the linear treatment breaks down. For typical plasma parameters in present-day tokamaks, the tearing layer is so thin that any visible magnetic island have to be in the nonlinear stage.

It is convenient to define the "helical flux",

$$\chi(r, \zeta) = -\int_{r_s}^{r}\left(1 - \frac{q}{q_s}\right) B_\theta dr + \psi(r)\cos\zeta \tag{6}$$

It is easily demonstrated that $(B + \delta B) \cdot \nabla\chi = 0$, so the contours of χ map out the perturbed magnetic flux surfaces. Close to the rational surface, Eqs. (2.3) and (2.6) yield

$$\Omega = \frac{\chi}{\Psi} = 8\frac{x^2}{W^2} + \cos\zeta \tag{7}$$

where $x = r - r_s$, and

$$W = 4\sqrt{\frac{R_0 q_s}{B_z s}\Psi} \tag{8}$$

Here, $s = (rq'/q)_{r=r_s}$ is the local magnetic shear, which is assumed to be positive.

Figure (4) shows contours of the normalized flux surface label Ω given by Eq. (7) plotted in (x, ζ) space.

An island structure of maximum radial width W is clearly shown. The island O-point is at coordinates $\Omega = -1, \zeta = \pi$, the separatrix corresponds to the $\Omega = 1$ contour, and the X-point is located at coordinates $\Omega = 1, \zeta = 0$. The perturbed flux surfaces are, of course, periodic in the helical phase angle ζ, repeating every 2π rads.

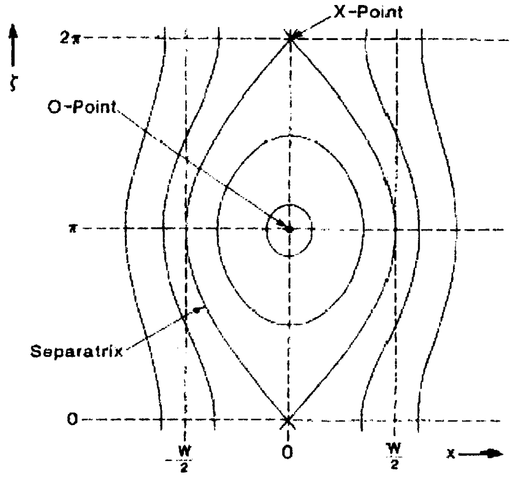

Fig. 4 Contours of the normalized flux surface label Ω plotted in (x, ζ) space, where x is the radial distance from the rational surface and ζ is the helical angle.

It is suggested that the nonlinearity is important principally in the singular layer around $k \cdot B = 0$, and in the case where the resistive skin diffusion time τ_R is much longer than the hydrodynamic time τ_H, the exponential growth of the field perturbation ψ is replaced by algebraic growth like t^2 at an amplitude of order $(\tau_H/\tau_R)^{4/5}$ [3].

The relative amplitudes of the $m = 4, 3$ and 2 modes shown in Fig. (5) are in fairly good agreement with the observations. Figure (5) also shows that there is a small interval of time when both the $m = 3$ and $m = 2$ modes are present; this occurs despite the fact that, according to the linear stability criteria, the $m = 3$ mode becomes stable before the onset of the $m = 2$. Nonlinearly, the $m = 3$ mode takes a certain time to relax after Δ' has become negative.

In neoclassical MHD tearing instabilities, tearing modes first grow exponentially in time. They next enter a $w\ \psi^{1/2}\ t^{1/2}$ growth regime where the bootstrap current contribution is important. For $\Delta' > 0$, they ultimately enter that Rutherford growth regime where the bootstrap current contribution is negligible [6].

Low mode number tearing type neoclassical MHD instabilities with $\Delta' > 0$ eventually evolve according

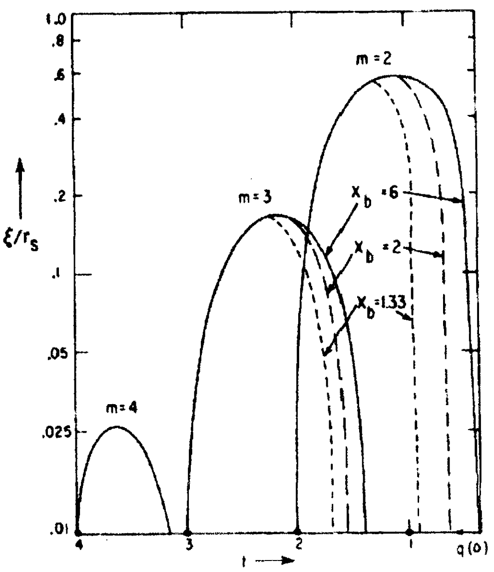

Fig. 5 Mode amplitude as functions of time for a constant current tokamak with shrinking current channel, and three locations x_b of the conducting shell. Amplitudes are expressed by the half-width ξ of the magnetic island in terms of their radii r_s. Good agreements with the observed amplitudes of the $m \geq 2$ oscillations are shown (quoted from [16]).

to the standard resistive MHD nonlinear theory. For higher mode numbers with $\Delta' < 0$, individual neoclassical MHD modes would saturate at the end of a $w\ t^{1/2}$ growth regime, but then the plasma becomes turbulent.

The saturated island width of the neoclassical tearing mode can be expressed as follows[1,9]:

$$w_{sat} \simeq -k_1 h(w) \sqrt{\epsilon} \beta_{p_s} \frac{L_q}{L_p} \frac{1}{\Delta'(w_{sat})} \tag{9}$$

where

$$k_1 \sim O(1)$$
$$h(w) = \frac{1}{1 + \left(\frac{w_d}{w}\right)^2}$$
$$w_d = 5.09 r_s \left(\frac{\chi_\perp}{\chi_l}\right)^{\frac{1}{4}} \left(\frac{1}{\epsilon_s s_s n}\right)^{\frac{1}{2}} \tag{10}$$

where $\epsilon_s, \beta_{p_s}, L_p, \chi_\perp$ and χ_l are inverse aspect ratio, poloidal beta, scale length of safety factor profile, scale length of pressure profile, diffusivity perpendicular to the magnetic field line and diffusivity parallel to the magnetic field line, respectively.

2.3 The Approach Based on Four-field Model

2.3.1 Linear Analysis

The linear analysis of NTM based on the four-field neoclassical MHD model is performed, in which the fluctuating ion parallel flow and ion neoclassical viscosity are newly taken into account [8]. The results from the four-field model are compared with those from the conventional three-field model which is with only the electron neoclassical viscosity. Figure (6) shows the collisionality dependence of the growth rate. In the three-field model case, NTM is unstable in the entire collisionality regime. On the other hand, in the case of the four-field model, the NTM is stabilized in the banana-plateau regime in spite of $\Delta' > 0$. This indicates that the fluctuating ion parallel flow and ion neoclassical viscosity have the stabilizing effect on the NTM.

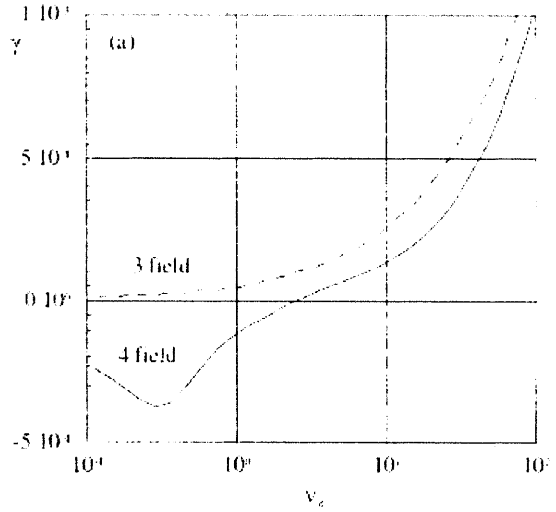

Fig. 6 The collisionality dependences of the growth rate. The solid line indicates the present four-field model including the ion and electron neoclassical viscosities. The dashed line indicates the conventional three-field model including only electron neoclassical viscosity. In the banana regime, this model has the negative growth rate compared with the three-field model (quoted from [16]).

2.3.2 Nonlinear Analysis

The dynamics of the magnetic island affected by the microscopic turbulence has been analyzed by using the renormalized reduced MHD equations with the cold ion approximation [9]. The evolution equations of the island width $w(t)$ and rotation frequency $\omega(t)$ are derived according to the Rutherford approach.

The island evolution equation is given by

$$\frac{G_1}{\eta}\frac{dw}{dt} = \frac{\Delta'}{4} + \frac{q^2}{s^2 w^3}\left(\frac{\hat\omega(\hat\omega-\hat\omega_*)}{\hat\omega-\hat\omega_*+\hat\omega_g}\right)^2 C_1 - \frac{q^2}{s^2 w}\frac{1}{\beta\hat\delta^2}\left(\frac{\hat\omega_g(\hat\omega_*-\hat\omega_g)(\hat\omega-\hat\omega_*)}{\hat\omega-\hat\omega_*-\hat\omega_g}\right) C_2 + \frac{\delta q^2}{sw\epsilon}\frac{m_e}{m_i}\frac{\mu_e}{\eta}\hat\omega_* G_2 \quad (11)$$

And the evolution equation for the rotation frequency is given by

$$\begin{aligned}
&\frac{\dot\omega}{w}\frac{\partial}{\partial\hat\omega}\frac{\hat\omega(\hat\omega-\hat\omega_*)}{\hat\omega-\hat\omega_*-\hat\omega_g}K_1 + \frac{w\dot\omega}{\delta^2\hat\beta}\frac{\hat\omega_g^2}{\hat\omega}\frac{\hat\omega_*-\hat\omega_g}{(\hat\omega-\hat\omega_*-\hat\omega_g)^2}K_2 \\
&-\frac{\dot w}{w^2}\frac{\hat\omega(\hat\omega-\hat\omega_*)}{\hat\omega-\hat\omega_*-\hat\omega_g}K_4 - \frac{\hat\omega_g\hat\omega}{\hat\omega}\frac{\dot w}{\delta^2\hat\beta}K_7 \\
&= -\frac{\hat\omega_g^2}{\hat\omega}\frac{\dot w}{\delta^2\hat\beta}K_7 + \hat\omega_*\delta\frac{m_e}{m_i}\frac{\hat\omega_g^2}{\hat\omega}\frac{1}{\delta^2\hat\beta}\frac{q^2}{sw\epsilon}\mu_e K_9 \\
&-\left(\frac{\hat\omega(\hat\omega-\hat\omega_*)}{\hat\omega-\hat\omega_*-\hat\omega_g}\right)^2\frac{\hat\omega_g^3(\hat\omega_*+\hat\omega_g)(\hat\omega-\hat\omega_*)}{\hat\omega(\hat\omega-\hat\omega_*-\hat\omega_g)}\frac{q^2}{s^2}\frac{1}{\delta^4\hat\beta^2}\frac{\eta_\parallel}{w}K_9 \\
&+\frac{1}{\delta^2\hat\beta}\frac{q^2}{s^2}\left(\frac{\hat\omega(\hat\omega-\hat\omega_*)}{\hat\omega-\hat\omega_*-\hat\omega_g}\right)^2\frac{\hat\omega_g^2}{\hat\omega}\frac{\hat\eta_\parallel}{w^3}K_{10} \\
&-\chi\frac{\hat\omega_g\hat\omega_*}{\hat\omega w}\frac{1}{\delta^2\hat\beta}K_1 - \frac{\mu}{w^3}\frac{\hat\omega(\hat\omega-\hat\omega_*)}{\hat\omega-\hat\omega_*-\hat\omega_g}K_{11}
\end{aligned} \quad (12)$$

The symbol of dot (as $\dot f$) indicates the time derivative. The numerical coefficients are given by $G_1 \sim 0.41, C_1 \sim 2.1, C_2 \sim 0.78, G_2 \sim 0.77$. And $K_1 \sim 33.7, K_2 \sim 5.45, K_4 \sim 26.0, K_7 \sim 2.44, K_9 \sim 1.03, K_{10} \sim 67.4, K_{11} \sim 22.5$.

Using Eqs.(2.11) and (2.12), a stability analysis is performed. Figure (7)(a) shows the stability of $\dot w$ in the (w,ω) plane. The solid curve indicates $\dot w = 0$. The grey arrow shows the rough direction of magnetic island evolution. In the shaded portion $0 < \hat\omega < \hat\omega_* + \hat\omega_g$, Eq.(2.12) does not have a solution which satisfies the boundary condition. It is found that the steady state solution of island width w_s is stable against the perturbation of island width δw. Figure (7)(b) shows the stability analysis of rotation frequency $\dot\omega$ in the (w,ω) plane. In contrast to the island width, the rotation frequency $\dot\omega$ has an only unstable solution to the perturbation of rotation frequency $\delta\omega$. If the rotation frequency exceeds the value of steady state solution, the rotation is accelerated. This leads to a disruption of the frequency in the end. Rutherford equation derived from four-field model has no steady state solution and the linear stability in four-field model is different from one in conventional three-field model. For these reasons, to investigate the onset condition and the mechanism of the island formation, the direct simulation of NTM by using four-field model is inevitable.

2.4 The Moment Approach to Neoclassical Theory

The theory of plasma transport in a torus relies mostly on kinetic theory ; the drift kinetic equation was solved rather than moment equations. A kinetic treatment was necessary since the mean-free path is long in the banana-plateau regime. Accordingly, Braginskii's collisional closure of the moment equations is not applicable. With kinetic, long-mean-free-path results in

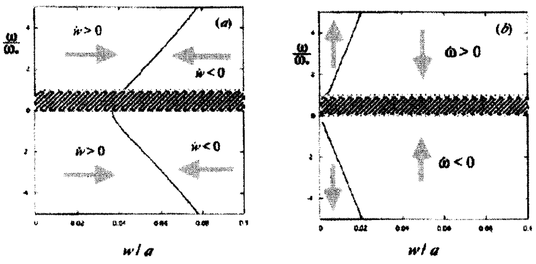

Fig. 7 The stabilities of $\dot{w}(a)$ and $\dot{\omega}(b)$ are shown in the (w, ω) plane. The solid curves indicate $\dot{w} = 0$ in (a) and $\dot{\omega} = 0$ in (b) respectively. The grey arrow the direction of the island evolution (quoted from [16]).

hand it is, however, now instructive to inspect their implications in terms of moment equations. Not only does this exercise shed light on the physics behind neoclassical transport, it is also highly useful in generalizing the theory to include the case of several ion species. The essential advantage of the moment approach to neoclassical transport in a multicomponent plasma is that it largely decouples the kinetics of different particle species from each other, which simplifies the calculations considerably. In this chapter we give a broad outline of the most important elements of the theory, which has been reviewed in full detail by Hirshman and Sigmar (1981).

2.4.1 The Parallel Viscous Force

We begin by recalling that the cross-field particle flux can be obtained by taking the toroidal projection of the momentum equation. After splitting off the classical flux (due to perpendicular fricton) and the $\mathbf{E} \times \mathbf{B}$ flux, the neoclassical flux remains

$$\langle \mathbf{\Gamma}_a \cdot \nabla\psi \rangle^{neo} \equiv -I \left\langle \frac{F_{a\parallel} + n_a e_a E_\parallel^{(A)}}{e_a B} \right\rangle$$

by using

$$\frac{\mathbf{B} \times \nabla\psi}{B^2} = \frac{I}{B}\mathbf{b} - R\hat{\psi}$$

$$\hat{\psi} = R\nabla\psi$$

We now decompose the latter into the *Pfirsh − Schlüter* flux and the *banana − plateau* flux,

$$\langle \mathbf{\Gamma}_a \cdot \nabla\psi \rangle^{neo} = \langle \mathbf{\Gamma}_a \cdot \nabla\psi \rangle^{PS} + \langle \mathbf{\Gamma}_a \cdot \nabla\psi \rangle^{BP}$$

with

$$\langle \mathbf{\Gamma}_a \cdot \nabla\psi \rangle^{PS} \equiv -I \left\langle \frac{R_{a\parallel} + n_a e_a E_\parallel^{(A)}}{e_a B} \left(1 - \frac{B^2}{\langle B^2 \rangle}\right) \right\rangle$$
$$\langle \mathbf{\Gamma}_a \cdot \nabla\psi \rangle^{BP} \equiv -I \frac{\left\langle B \left(R_{a_\parallel} + n_a e_a E_\parallel^{(A)}\right) \right\rangle}{e_a \langle B^2 \rangle} \tag{13}$$

Some details of these decompositions vary in the literature. The neoclassical heat flux is decomposed similarly, into

$$\langle \mathbf{q}_a \cdot \nabla\psi \rangle^{neo} = \langle \mathbf{q}_a \cdot \nabla\psi \rangle^{PS} + \langle \mathbf{q}_a \cdot \nabla\psi \rangle^{BP}$$

$$\begin{aligned} \langle \mathbf{q}_a \cdot \nabla\psi \rangle^{PS} &\equiv -IT_a \left\langle \frac{H_{a\parallel}}{e_a B} \left(1 - \frac{B^2}{\langle B^2 \rangle}\right) \right\rangle \\ \langle \mathbf{q}_a \cdot \nabla\psi \rangle^{BP} &\equiv -IT_a \frac{\langle B H_{a\parallel} \rangle}{e_a \langle B^2 \rangle} \end{aligned} \tag{14}$$

In this chapter we focus on the banana-plateau fluxes, which turn out to be dominant at low collisionality , $\nu \ll v_T/qR$, and large aspect ratio, $\epsilon \ll 1$.

The banana-plateau particle flux is driven by the *parallel viscous force*. To see this, we consider the scalar product of the momentum equation with $\mathbf{B}$, and take the flux-surface average. Since the time derivative is small in the transport ordering,

$$\frac{\partial}{\partial t} \sim \delta^2 \frac{v_T}{L}$$

we have

$$\left\langle B \left(R_{a\parallel} + n_a e_a E_\parallel\right) \right\rangle = \langle \mathbf{B} \cdot \nabla \cdot \mathbf{\Pi_a} \rangle \tag{15}$$

where we recall the vector notation $\mathbf{B} \cdot \nabla \cdot \mathbf{\Pi} = \Sigma_{j,k} \partial_k \Pi_{jk}$, and the definition

$$\Pi_{jk} \equiv \int m \left(v_j v_k - \frac{v^2}{3}\delta_{jk}\right) f d^3 v$$

We defined $\mathbf{\Pi}$ without the term $(v^2/3)\delta_{jk}$; this difference is unimportant here since this term does not survive the flux-surface average

$$\langle \mathbf{B} \cdot \nabla f(\psi, \theta) \rangle = 0$$

We also note that

$$\Pi_{jk} = \pi_{jk} + mnV_j V_k$$

Since we have assumed small flow velocities, $V \sim \delta v_T$, as is appropriate for most naturally occurring flows in a tokamak, Π is approximately equal to the usual viscosity π ; the difference is only $O(\delta^2 p)$, and we shall make no distinction between them. It is thus clear that the banana-plateau particle flux (13) is proportional to the parallel viscous force (15), averaged over the flux surface,

$$\langle \mathbf{\Gamma}_a \cdot \nabla\psi \rangle^{BP} \equiv -I \frac{\mathbf{B}\cdot\nabla\cdot\mathbf{\Pi}}{e_a\langle B^2\rangle} \tag{16}$$

In a completely analogous way, the heat flux across the flux surface, which is related to the heat friction by (14), as in

$$\frac{\langle \mathbf{q}_a \cdot \nabla\psi \rangle^{neo}}{T_a} = -\left\langle \frac{IH_{a\|}}{e_a B} \right\rangle$$

can be expressed in terms of the 'heat flux tensor'

$$\Theta_{jk} \equiv \int m\left(v_j v_k - \frac{v^2}{3}\delta_{jk}\right)\left(\frac{mv^2}{2T} - \frac{5}{2}\right) f d^3v$$

by

$$\langle \mathbf{q}_a \cdot \nabla\psi \rangle^{BP} \equiv -IT_a \frac{\langle BH_{a\|}\rangle}{e_a\langle B^2\rangle} = -IT_a \frac{\mathbf{B}\cdot\nabla\cdot\mathbf{\Theta_a}}{e_a\langle B^2\rangle} \tag{17}$$

The parallel viscous force can be related to a pressure anisotropy in the following way. We know that the distribution function f depends only weakly on the gyroangle ϑ,

$$\frac{\partial f}{\partial \vartheta} \sim \delta f$$

if the Larmor radius is small. Therefore, in a coordinate system aligned with the magnetic field, off-diagonal elements of Π are small. For instance, if the coordinates (x, y, z) are orthogonal, with z in the direction of $\mathbf{B}$, a typical off-diagonal element is

$$\Pi_{xy} = \int m v_x v_y f d^3v = \int m v_\perp^2 \sin\vartheta\cos\vartheta f d^3v = O(\delta)$$

Hence

$$\int m\mathbf{vv} f d^3v = \begin{pmatrix} p_\perp & 0 & 0 \\ 0 & p_\perp & 0 \\ 0 & 0 & p_\| \end{pmatrix} = p_\perp(\mathbf{I}-\mathbf{bb}) + p_\|\mathbf{bb}$$

Here, $\mathbf{I}$ is the unit tensor, $I_{jk} = \delta_{jk}, \mathbf{b} = \mathbf{B}/B$ is the unit vector in the direction of the magnetic field, and the parallel and perpendicular pressures are defined by

$$\begin{pmatrix} p_\| \\ p_\perp \end{pmatrix} = \int m \begin{pmatrix} v_\|^2 \\ v_\perp^2/2 \end{pmatrix} f d^3v$$

Note that the usual pressure is the mean of the pressure in the three perpendicular directions, $p = (2p_\perp^2 + p_\|)/3$. It now follows from the definition of Π that we can express this quantity in terms of the parallel and perpendicular pressures,

$$\begin{aligned} \mathbf{\Pi} &= p_\perp(\mathbf{I}-\mathbf{bb}) + p_\|\mathbf{bb} - p\mathbf{I} \\ &= (p_\| - p_\perp)\left(\mathbf{bb} - \frac{1}{3}\mathbf{I}\right) \end{aligned} \tag{18}$$

Finally, to evaluate $\langle \mathbf{B}\cdot\nabla\cdot\mathbf{\Pi}\rangle$, we note that for any scalar a, we have

$$\mathbf{B}\cdot\nabla\cdot(a\mathbf{I}) = \mathbf{B}\cdot\nabla a$$

and

$$\begin{aligned} \mathbf{B}\cdot\nabla\cdot(a\mathbf{bb}) &= B_j\partial_k(ab_jb_k) = B_jb_j\partial_k(ab_k) + B_jb_ka\partial_kb_j \\ &= B\nabla\cdot\left(\frac{a\mathbf{B}}{B}\right) + a\mathbf{B}\cdot[(\mathbf{b}\cdot\nabla)\mathbf{b}] \\ &= B^2\nabla_\|\left(\frac{a}{B}\right) = B\nabla_\| a - a\nabla_\| B \end{aligned}$$

where we have noted that the curvature $\kappa = (\mathbf{b}\cdot\nabla)\mathbf{b}$ is perpendicular to the magnetic field. The parallel viscous force thus becomes

$$\mathbf{B}\cdot\nabla\cdot\mathbf{\Pi} = (p_\perp - p_\|)\nabla_\| B + \frac{2}{3}B\nabla_\|(p_\| - p_\perp)$$

where the second term does not contribute to the flux-surface average.

$$\langle \mathbf{B}\cdot\nabla\cdot\mathbf{\Pi}\rangle = \langle (p_\perp - p_\|)\nabla_\| B\rangle \tag{19}$$

We conclude that the banana-plateau flux is driven by parallel variation of magnetic field strength, $\nabla_\| B \neq 0$, in combination with a difference between the parallel and perpendicular pressures. This difference can be written in terms of the Legendre polynomial $P_2(\xi) = (3\xi^2 - 1)/2$,

$$p_\| - p_\perp = \int mv^2 P_2(\xi) f d^3v \tag{20}$$

2.4.2 Plasma Flows

Parallel Viscosity Coefficients

As we have seen, the banana-plateau cross-field transport fluxes can be expressed in terms of parallel viscous forces. Our next step is to relate these forces to flows within the flux surface. It is required that (i) perpendicular fluxes are diamagnetic and (ii) total fluxes within the flux surface are divergence free. So we write the parallel fluxes of particles and heat as

$$V_{a\|} = V_{1a} + u_{a\theta}(\psi)B \tag{21}$$

$$q_{a\|} = \frac{5p_a}{2}V_{2a} + q_{a\theta}(\psi)B \tag{22}$$

where

$$V_{Ia} \equiv -\frac{1T_a}{m_a\Omega}\left(\frac{d\ln p_a}{d\psi} + \frac{e_a}{T_a}\frac{d\Phi}{d\psi}\right)$$

$$V_{2a} \equiv -\frac{I}{m_a\Omega_a}\frac{dT_a}{d\psi}$$

and

$$u_{a\theta}(\psi) = \frac{\mathbf{V}_a\cdot\nabla\theta}{\mathbf{B}\cdot\nabla\theta} \tag{23}$$

$$q_{a\theta}(\psi) = \frac{\mathbf{q}_a \cdot \nabla\theta}{\mathbf{B}\cdot\nabla\theta} \tag{24}$$

are contravariant components of the flow velocity and the heat flux. They are related to the notation in

$$n_a \mathbf{V}_a = \omega_a(\psi) n_a(\psi) R\hat{\varphi} + K_a(\psi)\mathbf{B} \tag{25}$$

and

$$\mathbf{q}_a = -\frac{5p_a}{2e_a B}\frac{dT_a}{d\psi}R\hat{\varphi} + L_a(\psi)\mathbf{B} \tag{26}$$

by $u_{a\theta} = K_a/n_a, q_{a\theta} = L_a$. Note that BV_{1a} and BV_{2a} are flux functions, so that the two terms in the parallel fluxes (25) and (26) vary over the flux surface in different ways. The first term is inversely proportional to B and the second term is directly proportional to B.

In general, the quantities $u_{a\theta}$ and $q_{a\theta}$ must be determined from kinetic theory. They are essentially the fluxes associated with the part g_a of the distribution function f_{a1} when the latter is decomposed as

$$f_{a1} = g_a + F_a \tag{27}$$

with F_a defined by

$$\begin{aligned} F_a &\equiv -\frac{Iv_\parallel}{\Omega_a}\frac{\partial f_{a0}}{\partial\psi} \\ &= -\frac{Iv_\parallel}{\Omega_a}\left[\frac{d\ln n_a}{d\psi} + \frac{e_a}{T_a}\frac{d\Phi}{d\psi} + \left(\frac{m_a v^2}{2T_a} - \frac{3}{2}\right)\frac{d\ln T_a}{d\psi}\right] f_{a0} \end{aligned}$$

Indeed, if g_a is expanded in Sonine polynomials,

$$g_a = f_{a0}\frac{m_a v_\parallel}{T_a}\sum_{j=0}^{\infty} u_{aj} L_j^{3/2}(x^2) \tag{28}$$

then

$$\begin{aligned} u_{a0} &= u_{a\theta}(\psi)B \\ u_{a1} &= -\frac{2}{5p_a}q_{a\theta}(\psi)B \end{aligned} \tag{29}$$

It is clear that if the coefficients u_{aj} of all species were known, we would have complete knowledge of the distribution functions, and we could thus calculate the friction force $R_{a\parallel}$, or equivalently, the parallel viscous force by (15). In a similar way, the heat friction $H_{a\parallel}$ and the heat flux tensor Θ could also be calculated. In practice, sufficient accuracy is often obtained by including only the first two terms. This truncation is known as the 13-moment approximation in the literature on kinetic gas theory. Hence, the basic problem of neoclassical theory is to calculate the coefficients u_{aj} in

$$\langle \mathbf{B}\cdot\nabla\cdot\mathbf{\Pi_a}\rangle = 3\left\langle(\nabla_\parallel B)^2\right\rangle\left(\mu_{a1}u_{a\theta} + \mu_{a2}\frac{2q_{a\theta}}{5p_a}\right) \tag{30}$$

$$\langle \mathbf{B}\cdot\nabla\cdot\mathbf{\Theta_a}\rangle = 3\left\langle(\nabla_\parallel B)^2\right\rangle\left(\mu_{a2}u_{a\theta} + \mu_{a3}\frac{2q_{a\theta}}{5p_a}\right) \tag{31}$$

where the overall multiplier $3\left\langle(\nabla_\parallel B)^2\right\rangle$ has been chosen in order to match to Braginskii's terminology in the appropriate limit. The unknown coefficients μ_{aj} are often referred to as *neoclassical parallel viscosity coefficients* and summarize most of the kinetic information necessary to evaluate the neoclassical transport. It is sometimes practical to write them as

$$\begin{aligned} \mu_{a1} &= K_{11}^a \\ \mu_{a2} &= K_{12}^a - \frac{5}{2}K_{11}^a \\ \mu_{a3} &= K_{22}^a - 5K_{12}^a + \frac{25}{4}K_{aa}^a \end{aligned} \tag{32}$$

The new coefficients K_{jk}^a thus defined turn out to be positive definite and are easier to interpolate between different collisionality regimes.

Parallel Flow

We now use neoclassical parallel viscosity coefficients to construct the parallel flow velocity in a torus with large aspect ratio, $\epsilon \ll 1$. In this limit the parallel flow velocities of all species are approximately equal and parallel heat fluxes are small (compared with $n_a T_a V_{1a}$ or $n_a T_a V_{2a}$). This is intuitvely clear from the circumstance that in a cylinder (the limit $\epsilon \to 0$) all species must share a common parallel flow velocity. There is then no toroidicity to drive a particle flow or a heat flux in either direction along the field. In a torus, the relative flow velocity between different species is finite but small if $\epsilon \ll 1$. It is of order $O(\epsilon^{1/2})V_1$, and we can thus write

$$\langle V_{a\parallel}B\rangle \simeq \langle VB\rangle \tag{33}$$

$$\langle q_{a\parallel}B\rangle \simeq 0 \tag{34}$$

where V is the same for all species if ϵ is small. This common flow V can be determined from momentum balance,

$$\sum_a \langle \mathbf{B}\cdot\nabla\cdot\mathbf{\Pi_a}\rangle = \sum_a \left\langle B\left(R_{a\parallel} + n_a e_a E_\parallel\right)\right\rangle = 0$$

where we substitute (21), (22) and (30), and solve for V,

$$V = \frac{\sum(\mu_{a1}V_{1a} + \mu_{a2}V_{2a})}{\sum \mu_{a1}}$$

As the viscosity coefficients turn out to be smaller for electrons than for ions by the ratio $(m_e/m_i)^{1/2}$, only the latter need to be included in the sums over species index a. In a pure plasma with only one ion species, we have simply

$$V = V_{1i} + \frac{\mu_{i2}}{\mu_{i1}}V_{2i}$$

Hence and from (21) it follows that, in such a plasma, the poloidal flow velocity is simply proportional to the temperature gradient,

$$V_{i\theta} = \mu_{i\theta}(\psi)B = V_{i\parallel} - V_{1i} = \frac{\mu_{i2}}{\mu_{i1}}V_{2i} \tag{35}$$

We also note that the parallel and toroidal flow velocities within the flux surface depend on density and temperature gradients as well as on the radial electric field (through $d\Phi/d\psi$ in V_{1a}). The latter does not affect cross-field fluxes (as long as it is small enough to comply with our orderings, which preclude sonic flows), to which we now turn our attention.

Cross-field Transport

When the aspect ratio is large and the collisionality low the largest contribution to cross-field transport comes from the banana-plateau fluxes (16), (17). These fluxes can be obtained directly from the fundamental relations (17), (18) once the poloidal flows are known. In the approximation (33), (21), which holds for $\epsilon \to 0$, the latter are given by

$$u_{a\theta}(\psi) = \frac{\langle (V - V_{1a})B\rangle}{\langle B^2\rangle}$$

$$\frac{2q_{a\theta}(\psi)}{5p_a} = -\frac{V_{2a}B}{\langle B^2\rangle}$$

Note that although the radial electric field enters through $d\Phi/d\psi$ in V_{1a} it disappears from the poloidal flow $u_{a\theta}$ and from the banana-plateau cross-field fluxes of particles and heat, Eqs. (16) and (17), which become

$$\langle \mathbf{\Gamma}_a \cdot \nabla\psi\rangle^{BP} = -3\left\langle (\nabla_\parallel B)^2\right\rangle \frac{IB}{e_a B_0^4} \times \left[\frac{\mu_{a1}}{\mu_1}\sum_b(\mu_{b1}V_{1b} + \mu_{b2}V_{2b}) - \mu_{a1}V_{1a} - \mu_{a2}V_{2a}\right]$$

$$\langle \mathbf{q}_a \cdot \nabla\psi\rangle^{BP} = -3\left\langle (\nabla_\parallel B)^2\right\rangle \frac{IT_a B}{e_a B_0^4} \times \left[\frac{\mu_{a2}}{\mu_1}\sum_b(\mu_{b1}V_{1b} + \mu_{b2}V_{2b}) - \mu_{a2}V_{1a} - \mu_{a3}V_{2a}\right]$$

with $B_0^2 = \langle B^2\rangle$ and

$$\mu_1 \equiv \sum_a \mu_{a1}$$

Finally, these transport laws may be summarized in a compact form by introducing the thermodynamic forces

$$A_1^a \equiv \frac{d\ln p_a}{d\psi} + \frac{e_a}{T_a}\frac{d\Phi}{d\psi}$$
$$A_2^a \equiv \frac{d\ln T_a}{d\psi}$$

so that $V_{ja} = -(IT_a/e_aB)A_1^a$, and the cross-field fluxes

$$I_1^a \equiv \langle \mathbf{\Gamma}_a \cdot \nabla\psi\rangle^{BP}$$
$$I_2^a \equiv \langle \mathbf{q}_a \cdot \nabla\psi\rangle^{BP}/T_a$$

Their relation to one another is then given by

$$I_j^a = \sum_{b,k} L_{jk}^{ab} A_k^b$$

$$L_{jk}^{ab} = 3\left\langle (\nabla_\parallel B)^2\right\rangle \frac{I^2 T_b}{e_a e_b B_0^4}\left(\frac{\mu_{aj}\mu_{bk}}{\mu_1} - \mu_{a,j+k-1}\delta_{ab}\right) \tag{36}$$

Note that the transport coefficients $L_{jk}^{ab} = L_{kj}^{ab}$ are Onsager symmetric. These laws essentially summarize the neoclassical transport of a plasma with an arbitrary number of ion species. All kinetic information necessary to evaluate the transport at large aspect ratio is contained in the velocity coefficients μ_{aj}. The advantage of this formulation is that the viscosity coefficients can be determined relatively easily for one species at a time since they depend on the other species only through collision frequencies. The fluxes are more complex quantities, depending in a complicated way on the parallel flows of all species.

3. Numerical Analysis of Neoclassical Tearing Mode

3.1 Model Equations

We consider a high temperature plasma of major and minor radii R_0 and a with a troidal magnetic field B_0 in the cylindrical coordinates (r, θ, z). To analyze NTM, we use the four-field reduced neoclassical MHD model [8]. This model consists of
the vorticity equation:

$$\begin{aligned}&\frac{\partial}{\partial t}\nabla_\perp^2 F + [F, \nabla_\perp^2 F] - \alpha_i \nabla_\perp F \cdot [p, \nabla_\perp F]\\ &= -\nabla_\parallel \nabla_\perp^2 A - [\Omega, p] + \mu_i^{cl}\nabla_\perp^4 F\\ &\quad - \frac{q}{\epsilon}\mu_i^{neo}\frac{\partial U_{pi}}{\partial r} - \frac{q}{\epsilon}\frac{m_e}{m_i}\mu_e^{neo}\frac{\partial U_{pe}}{\partial r}\end{aligned} \tag{37}$$

Ohm's law:

$$\begin{aligned}\frac{\partial A}{\partial t} &= -\nabla_\parallel(\phi - \alpha_e p) + \alpha^2\frac{m_e}{m_i}[\phi, \nabla_\perp^2 A]\\ &\quad + \eta_\parallel^{cl}\nabla_\perp^2 A + \alpha\frac{m_e}{m_i}\mu_e^{neo}U_{pe}\end{aligned} \tag{38}$$

the evolution of pressure:

$$\begin{aligned}&\frac{\partial}{\partial t}p + [\phi, p]\\ &= \hat{\beta}([\Omega, \phi - \alpha_e p] - \nabla_\parallel(v_\parallel + \alpha\nabla_\perp^2 A)\\ &\quad + \eta_\perp^{cl}\nabla_\perp^2 p - \alpha\frac{m_e}{m_i}\frac{q}{\epsilon}\mu_e^{neo}\frac{\partial U_{pe}}{\partial r})\end{aligned} \tag{39}$$

the evolution of ion parallel velocity:

$$\frac{\partial}{\partial t}v_{\parallel} + [\phi, v_{\parallel}] = -\nabla_{\parallel}p + 4\mu_i^{cl}\nabla_{\perp}^2 v_{\parallel} - \mu_i^{neo}U_{pi} - \frac{m_e}{m_i}\mu_e^{neo}\frac{\partial U_{pe}}{\partial r} \tag{40}$$

where

$$F = \phi + \alpha_i p \tag{41}$$

$$U_{pi} = v_{\parallel} + \frac{q}{\epsilon}(\phi + \alpha_i p) \tag{42}$$

$$U_{pe} = v_{\parallel} + \alpha\nabla_{\perp}^2 A + \frac{q}{\epsilon}(\phi - \alpha_e p) \tag{43}$$

$$\Omega = 2r\cos\theta, \hat{\beta} = \frac{\beta}{1+\beta}, \alpha = \frac{c}{a\omega_{pi}}$$

$$\alpha_i = \frac{T_i}{T_i + T_e}\alpha, \alpha_e = \frac{T_e}{T_i + T_e}\alpha$$

and

$$\nabla_{\parallel} = \frac{\partial}{\partial z} - [A,] \tag{44}$$

The variables $\{\phi, A, p, v_{\parallel}\}$ are the fluctuating electrostatic potential, vector potential parallel to the magnetic field, pressure and parallel velocity, respectively. In this model, the ion and electron temperatures T_i and T_e are assumed to be constant and uniform and $T_i = T_e$. The coefficients $\mu_i^{cl}, \eta_{\parallel}^{cl}, \eta_{\perp}^{cl}$ are classical ion viscosity, resistivity and diffusivity, respectively. F is the generalized potential, U_{pi} and U_{pe} are the fluctuating ion and electron neoclassical flows. α is the normalized ion skin depth, and Ω is the normalized magnetic curvature, which introduces the ballooning coupling. $q, \epsilon, \omega_{pi}, \beta$ indicate the safety factor, the inverse aspect ratio, ion plasma frequency and plasma beta value, respectively. The Poisson bracket is defined by $[f, g] = \mathbf{b}\cdot\nabla f \times \nabla g$ where $\mathbf{b}$ is an unit vector parallel to the magnetic field. These equations are normalized by the toroidal Alfven times and minor radius, respectively; $v_A t/R \to t$, $r/a \to r$. The energy balance is written by

$$\frac{dH}{dt} = -\int dv\Big(\mu_i^{cl}\left|\nabla_{\perp}^2 F\right|^2 + \eta_{\parallel}^{cl}\left|\nabla_{\perp}^2 A\right|^2 + 4\mu_i^{cl}\left|\nabla_{\perp}v_{\parallel}\right|^2 + \eta_{\perp}^{cl}\left|\nabla_{\perp}p\right|^2 + \mu_i^{neo}\left|U_{pi}\right|^2 + \frac{m_e}{m_i}\mu_e^{neo}\left|U_{pe}\right|^2\Big) \tag{45}$$

where the Hamiltonian H is given by

$$H = \frac{1}{2}\int dv\left(\left|\nabla_{\perp}F\right|^2 + \left|\nabla_{\perp}A\right|^2 + \left|v_{\parallel}\right|^2 + \frac{|p|^2}{\hat{\beta}}\right) \tag{46}$$

3.2 Viscosity Model

In the four-field reduced neoclassical MHD model, we approximated parallel and cross viscous stress tensor terms as

$$\mathbf{b}\cdot\nabla\cdot\Pi_{\parallel z} \simeq m_z n_z \mu_z B^2 U_{pz} \tag{47}$$

$$\nabla\cdot(\mathbf{b}\times\nabla\cdot\Pi_{\parallel z}) \simeq -\frac{B_0}{B_\theta}\frac{\partial}{\partial r}(\mathbf{b}\cdot\nabla\cdot\Pi_{\parallel}z) \tag{48}$$

where the subscript z denotes species of charged particle, and the neoclassical viscosities are given by the interpolated formula [13] as

$$\mu_e^{neo} = \frac{2.3\sqrt{\epsilon}\nu_e}{(1 + 1.07\nu_{*e}^{1/2} + 1.02\nu_{*e})(1 + 1.07\nu_{*e}\epsilon^{3/2})} \tag{49}$$

$$\mu_i^{neo} = \frac{0.66\sqrt{\epsilon}\nu_i}{(1 + 1.03\nu_{*i}^{1/2} + 0.31\nu_{*i})(1 + 0.66\nu_{*i}\epsilon^{3/2})} \tag{50}$$

where

$$\nu_{*s} = \nu_s qR/(\epsilon^{3/2}v_{ths})$$

In a realistic parameter range of present experiments and future reactors, NTM might occur in the banana regime, however in simulation, we use $\eta_{\parallel}^{cl} = 10^{-7} \sim 10^{-5}$ which corresponds to the Pfirsh-Schlüter and plateau regime. Then, for nonlinear simulations, we need somewhat larger value of viscosity, otherwise, smaller mesh grid and time step are required. Such simulations are expensive and time-consuming so that only a few simulations are possible.

For this reason, instead of using the above formula of neoclassical viscosity, in this thesis, we employ two types of model viscosity which are shown in Fig. 8. We call (1) Banana viscosity model, and (2) HS viscosity model. The Banana viscosity model (1) is an idealized model where the viscosity in the banana regime is extended to the plateau and Pfirsh Schluter regime. For this model, the neoclassical viscosities in PS regime are given by

$$\mu_e^{neo} = 2.3\sqrt{\epsilon}\mu_e, \quad \mu_i^{neo} = 0.66\sqrt{\epsilon}\mu_i. \tag{51}$$

On the other hand, the HS viscosity model (2) is based on the Hirshman-Sigmar formula [13]. For this model, neoclassical viscosities in PS regime is given by

$$\mu_e^{neo} = 2.1\sqrt{\epsilon}\frac{\mu_{be}\mu_{pe}}{\mu_e}, \quad \mu_i^{neo} = 3.2\sqrt{\epsilon}\frac{\mu_{bi}\mu_{pi}}{\mu_i}. \tag{52}$$

3.3 Safety Factor and Plasma Parameter

As the standard case of numerical simulations, we set the following form of safety factor profile as the initial condistion;

$$q(r) = q_0\left(1 + \left(\frac{r}{r_s}\right)^2\right), \tag{53}$$

where $q_0 = 1.01$ and $r_s = 0.56$. Then the shear parameter, at the rational surface r_s is evaluated by

$$s = \frac{r_s}{q(r_s)}\frac{dq(r_s)}{dr_s}. \tag{54}$$

This q profile is unstable against the classical tearing mode, that is $\Delta' > 0$, where Δ' is defined by

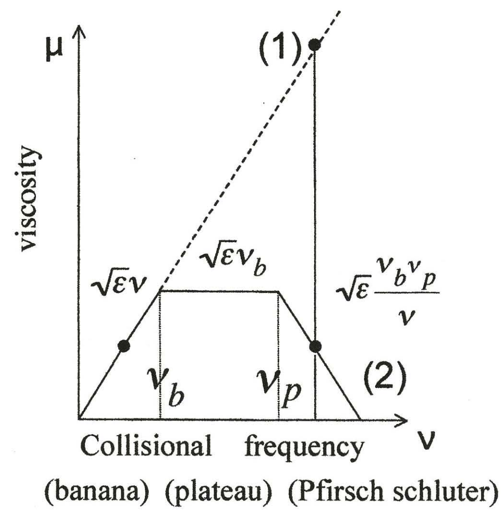

Fig. 8 Viscosity model: We use two models; (1) B model and (2) HS model. B model is an idealized model where the viscosity in the banana regime is extended to the plateau and Pfirsh-Schluter regime on the other hand, HS model is based on the Hirshman-Sigmar formula. B model is adopted in order to solve problems characteristic of numerical simulations for expressing NTM.

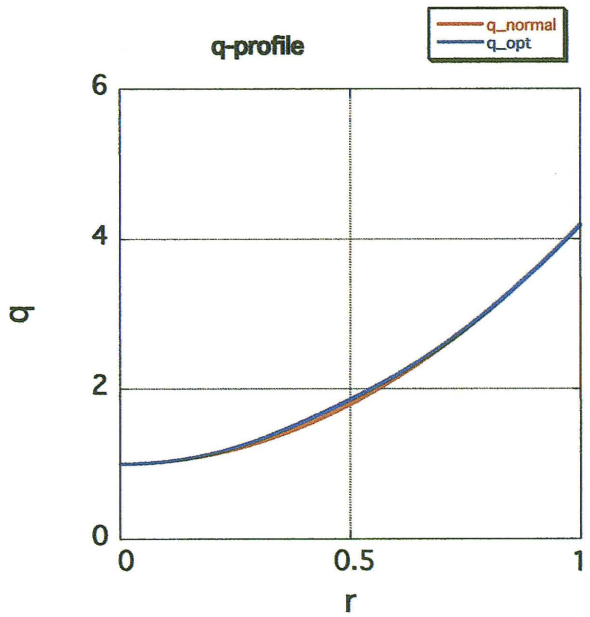

Fig. 9 Safety factor profile: We use two types of safety factor profiles; (1) the normal q profile ($\Delta' > 0$) and (2) the optimized q profile ($\Delta' = 0$). The red curve indicates the normal q profile and the blue curve indicates the optimized q profile. The optimized q profile is adopted in order to exclude the effect of the classical tearing mode at the initial phase.

$$\Delta' = \frac{A'(+\delta) - A'(-\delta)}{A(0)}.$$

If $\Delta' > 0$, then the tearing mode is unstable and if $\Delta' < 0$, it is stable.

In order to exclude the effect of the classical tearing mode at the initial phase, we also use the q profile, which is optimized so that $\Delta' = 0$. This q profile is refered as the optimized q profile. Fig. 9 show these two initial q profiles. There is a small difference between them around the rational surface.

The initial pressure profile is given by

$$p(r) = \frac{\beta}{\epsilon}(1-r)^2 \tag{55}$$

where $\epsilon = a/R_0 = 1/3$, $\beta = 0.01$.

We also fix $\alpha = 0.01$ in the following simulations.

3.4 Linear Analysis

To analyze linear NTM, a perturbed quantity $f(\mathbf{x}, t)$ is assumed to vary as $f_{m,n}(r)\exp[im\theta+in\zeta+(\gamma-i\omega)t]$ in the cylindrical coordinates, where m is a poloidal mode number, n is a troidal mode number, γ is the growth rate and ω is the frequency of the linear tearing mode. The direction of $\omega > 0$ corresponds to the electron diamagnetic drift direction and of $\omega < 0$ to the ion diamagnetic drift direction. $f_{m,n}(r)$ satisfies the boundary conditions; $f_{m,n}(0) = 0$ and $f_{m,n}(a) = 0$. In this study, a single helicity mode with $m/n = 2$ is considered. The basic Eqs. (3.1)-(3.4) are linearized and the linear contribution from the ion convective term and gyro-viscous term in the vortisity equation is evaluated as

$$\begin{aligned}&[F, \nabla_\perp^2 F] - \alpha_i \nabla_\perp \cdot [p, \nabla F]\\ &= \frac{\alpha_i}{r}\left(-\frac{d^3 p_0}{dr^3}\frac{\partial\phi}{\partial\theta} + \frac{dp_0}{dr}\frac{1}{r}\frac{\partial^2\phi}{\partial\theta\partial r} - \frac{d^2 p_0}{dr^2}\frac{\partial^2\phi}{\partial\theta\partial r}\right)\end{aligned} \tag{56}$$

where p_0 is the equilibrium pressure profile.

3.5 Nonlinear Simulation

The four-field equations are solved by the mixture of finite difference and spectral method. A perturbed quantity is decomposed by $f(r,\theta,z,t) = \sum_{m,n} f_{m,n}(r,t)e^{im\theta - imz}$. In r direction, the finite difference method is used, and in θ , z direction, Fourier expansion method is employed. The boundary condition is given by $f_{m,n}(0) = 0$, $f_{m,n}(a) = 0$ and $f'_{0,0}(0) = 0$, $f_{0,0}(a) = 0$. The perturbed energy are defined by

$$E_F = \sum_{m,n} E_F(m,n) \ , \quad E_F(m,n) = \frac{1}{2} = \int |\nabla F|^2 \, dr$$
$$E_A = \sum_{m,n} E_A(m,n) \ , \quad E_A(m,n) = \frac{1}{2} = \int |\nabla A|^2 \, dr$$
$$E_p = \sum_{m,n} E_p(m,n) \ , \quad E_p(m,n) = \frac{1}{2\beta} = \int |p|^2 \, dr$$
$$E_{v_\parallel} = \sum_{m,n} E_{v_\parallel}(m,n) \ , \quad E_{v_\parallel}(m,n) = \frac{1}{2} = \int |v_\parallel|^2 \, dr \tag{57}$$

Using these quantity, we investigate the time evolution of perturbed energies.

4. Simulation Results

4.1 Linear Analysis

4.1.1 Dependence of the Growth Rate on the Viscosity Model and the q Profile

The dependence of neoclassical viscosity (μ_{neo}) on the resistivity ($\eta_\parallel^{cl}$) is shown in Fig. (10). The opposite dependence on the resistivity is observed for B model and HS model; viscosity μ_{neo} is an increasing function of $\eta_\parallel^{cl}$ for B model on the other hand μ_{neo} is decreasing function of $\eta_\parallel^{cl}$ for HS model. This is because $\eta \simeq 10^{-7}$ is laid on the plateau region, so that HS model shows plateau and Pfirsch-Schlüter nature. On the other hand, B model shows the banana nature.

Figure (11) shows the dependence of growth rate on the toroidal mode number n in the case with normal q profile. The (2,1) mode is stable for HS model with $\eta \simeq 10^{-7}$ (see in Fig.(6)), on the other hand, it is unstable for B model in the range of $10^{-7} \leq \eta \leq 10^{-5}$. According to an increase of neoclassical viscosity, the (2,1) mode is stabilized in HS model, while it tends to be destabilized for B model. All high n modes are stable in HS model, which indicates the nature of classical tearing mode, while it is unstable in B model. It is found that the high n mode is more unstable than (2,1) mode. The collisional drift wave might be driven by enhanced neoclassical viscosity for B model. We obtain the relation of $\gamma \propto \left(\eta_\parallel^{cl}\right)^{1/3} n^{2/3}$ by fitting of numerical results in Fig. (11), which agree with the theoretical prediction [17].

Next, we investigate an instability source of B model. Fig. (12) shows the dependence of the growth rate on the electron neoclassical viscosity for B model. The blue curve indicates the growth rate of (2,1) mode, and the red curve indicates that of (20,10) mode, respectively. Since a relation of $\mu_e^{neo} \propto \eta_\parallel^{cl}$ is hold in B model, μ_e^{neo} is changed with fixed $\eta_\parallel^{cl}$ to separate these two effect. It is shown that both growth rates increase with the μ_e^{neo} increase, and following relation is obtained, $\gamma_{1/2} \propto (\mu_e^{neo})^{3/4}$ and $\gamma_{10/20} \propto (\mu_e^{neo})^{4/5}$ by fitting.

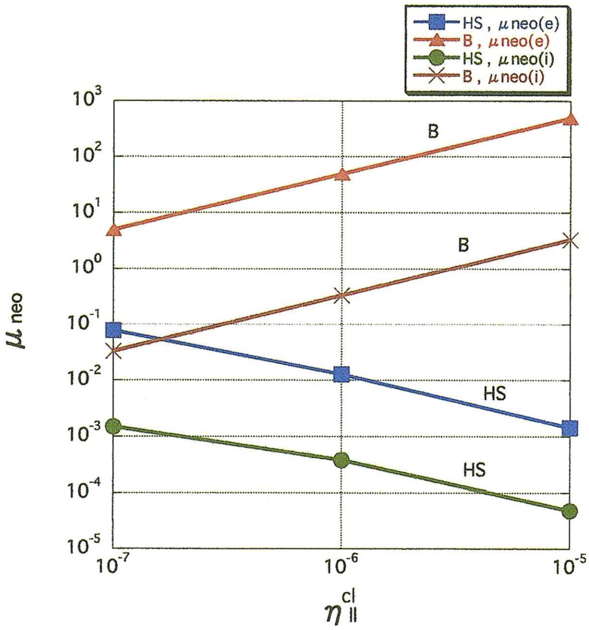

Fig. 10 μ_{neo} dependence on $\eta_\parallel^{cl}$: This figure shows the dependence of neoclassical viscosity (μ_{neo}) on the resistivity ($\eta_\parallel^{cl}$). For HS model, both μ_e^{neo} and μ_i^{neo} decrease according to an increase of $\eta_\parallel^{cl}$ on the other hand, for B model, both μ_e^{neo} and μ_i^{neo} increase with an increase of $\eta_\parallel^{cl}$. μ_{neo} dependence on $\eta_\parallel^{cl}$ is different for each viscosity model.

It is found that the (20,10) mode has more strong dependence on the neoclassical viscosity compared with the (2,1) mode, which indicates the collisional drift wave nature of high n modes.

Finally, the relation of $\gamma_{1/2} \propto \left(\eta_\parallel^{cl}\right)^{-5/12} (\mu_e^{neo})^{3/4}$ is obtained by using these results.

Figure (13) show the dependence of growth rate on the toroidal mode number n in the case with the optimized q profile. The same value of neoclassical viscosity are used for these calculations. For the HS model, the (2,1) mode becomes stable for $\eta = 10^{-5}$ and $\eta = 10^{-6}$ due to the optimized q profile, i.e. , $\Delta' = 0$. On the other hand, the (2,1) mode is unstable for the B model in the range of $10^{-7} \leq \eta \leq 10^{-5}$. It is found that the growth rate of high n mode is larger than that of normal q profile in B model, however, whole tendency is not changed. The optimization of q profile destabilizes not only TM but also the collisional drift wave driven by neoclassical viscosity for B model. Therefore, the modeling of dissipation is quite important to examine the NTM dynamics.

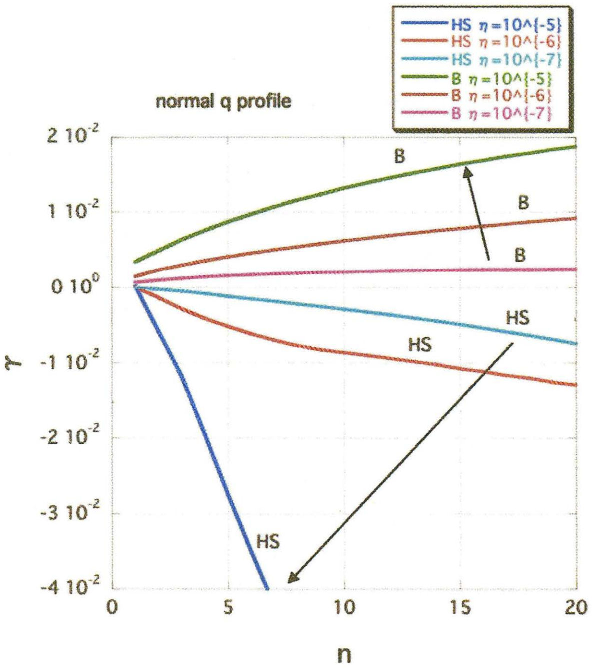

Fig. 11 Dependence of growth rate (γ) on the toroidal mode number (n) in the case with the normal q profile: The (2,1) mode is unstable for HS model with $\eta_{\|}^{cl} > 10^{-7}$ on the other hand it is unstable for B model in the range of $10^{-7} \le \eta_{\|}^{cl} \le 10^{-5}$. High n mode is stable in HS model, which indicates the nature of classical tearing mode, while it is unstable in B model.

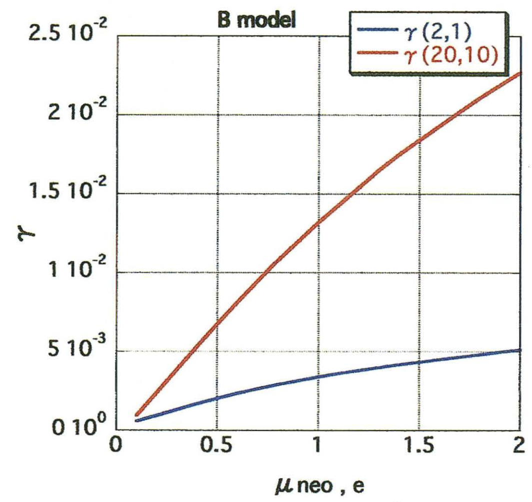

Fig. 12 The electron neoclassical viscosity dependence of the growth rate for B model: The blue curve indicates the growth rate of (2,1) mode, and the red curve indicates that of (20,10) mode, respectively. Since a relation of $\mu_e^{neo} \propto \eta_{\|}^{cl}$ is formed in B model, μ_e^{neo} is changed with fixed $\eta_{\|}^{cl}$. Both growth rates increase with the μ_e^{neo} increase, and following relation is formed, $\gamma_{1/2} \propto (\mu_e^{neo})^{3/4}$ and $\gamma_{10/20} \propto (\mu_e^{neo})^{4/5}$.

4.1.2 Dependence of the Frequency on Viscosity Model and q Profile

Figure (14) shows the dependence of frequency on toroidal mode number n. It is shown that the frequency depends on the viscosity model. Here, $\omega < 0$ indicates an electron diamagnetic direction and $\omega > 0$, an ion diamagnetic direction. The frequency of (2,1) mode in case with $\eta = 10^{-5}$ and $\eta = 10^{-6}$ for HS model is in the electron diamagnetic direction ($\omega < 0$) while it is almost zero in the case with $\eta = 10^{-7}$. The frequencies of high n modes are deeply in the electron diamagnetic direction in cases with $\eta = 10^{-5}$ and $\eta = 10^{-6}$. In the case with $\eta = 10^{-7}$, the frequencies with middle n modes are in the ion diamagnetic direction and those with high n modes are in the electron diamagnetic direction. The similar tendency as for B model is observed in the middle n mode, however, high n mode shows the nature for HS model with $\eta = 10^{-5}$ and 10^{-6}.

Figure (15) shows dependence of the frequency on the toroidal mode number n in the case with the optimized q profile. The similar tendency is observed as the case with normal q profile. The (2,1) mode frequency in the case of HS model with $\eta = 10^{-6}$ is almost zero and the direction of propagation of high n modes are in the electron diamagnetic direction. From Figs. (14) and (15), frequencies of high n modes shift to the ion diamagnetic direction according to the increase of neoclassical viscosity of B model, on the other hand, frequencies of high n modes are sensitive to the q profile for HS model. For B model, the similar tendency is observed for three cases. The frequency increases in the ion diamagnetic direction according to the increase of n. It is considered that this the unstable high n mode has the property of the collisional ion drift wave.

4.2 Nonlinear Simulation

The nonlinear simulations are performed for two cases :

1. HS model with $\eta = 10^{-5}$ and normal q profile, which corresponds to the nonlinear simulation of TM.
2. B model with $\eta = 10^{-5}$ and normal q profile, which corresponds to the nonlinear simulation of NTM and collisional ion drift waves.

It should be noted that a slightly different q profile is used for these simulations compared with those in the previous section, i.e., Eq. (53) with $q_0 = 1.2$ and $r_s = 0.6$.

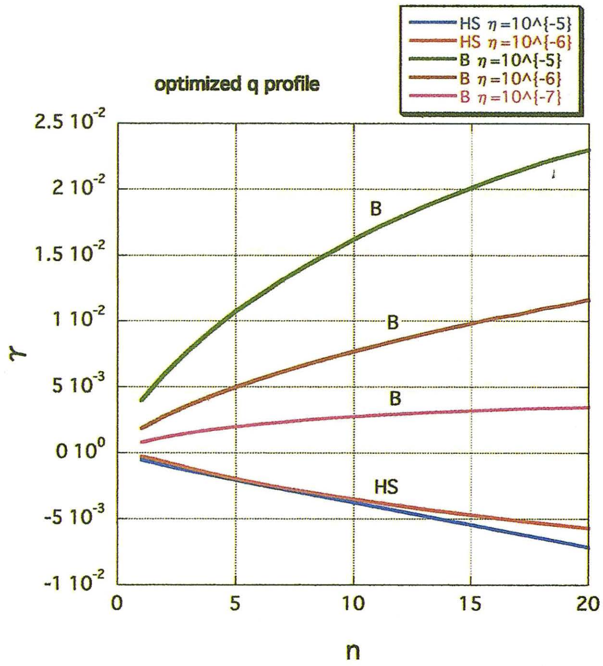

Fig. 13 Dependence of growth rate (γ) on the toroidal mode number (n) in the case with the optimized q profile: For HS model, the (2,1) mode becomes stable for $\eta_{\parallel}^{cl} = 10^{-6}$ and $\eta_{\parallel}^{cl} = 10^{-5}$ due to $\Delta' = 0$. On the other hand, the (2,1) mode is unstable for B model in the range of $10^{-7} \leq \eta_{\parallel}^{cl} \leq 10^{-5}$.

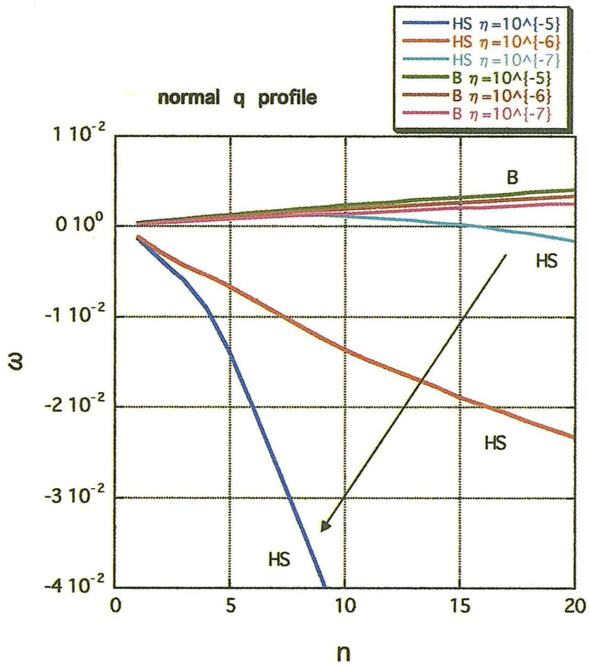

Fig. 14 Dependence of frequency ω on toroidal mode number n: $\omega < 0$ indicates an electron diamagnetic direction and $\omega > 0$, an ion diamagnetic direction. The (2,1) mode frequency in the case with $\eta_{\parallel}^{cl} = 10^{-6}$ and $\eta_{\parallel}^{cl} = 10^{-5}$ for HS model is in the electron diamagnetic direction. Frequencies of high n modes shift to the ion diamagnetic direction according to the increase of neoclassical viscosity of B model, on the other hand, frequencies of high n modes are sensitive to the q profile for HS model.

Figures (16) and (17) show temporal evolutions of fluctuation energy for the cases with HS model and with B model, respectively. Each energy is given by Eq. (57), where the blue curve represents E_p, the green curve E_A, the brown curve $E_{v_{\parallel}}$ and the orange curve E_F. E_p and E_A are dominant in the total energy. In the case with HS model, the linear growth and quasi-linear saturation is attained as is seen in Fig. (16). On the other hand, in the case with B model, two step saturation is observed. The TM growth is driven by the beat interaction of high n modes so that the linear growth rate of TM plays no role in the growing phase $t \lesssim 1000$. Then the first saturation is observed at $t \simeq 1000$. In this phase, the high n collisional drift waves are saturated at the low amplitude, and TM continues to grow. At $t \simeq 5000$, the second saturation is observed where TM is saturated quasi-linearly. This time is almost half of that in HS model. It is conjectured that high n drift wave accelerates the growth of TM via nonlinear beat interaction so that the linear time scale of TM is not important anymore in this simulation.

Figures (18) and (19) show the temporal evolution of electromagnetic energy of each Fourier mode for the cases with HS and B models, respectively. For HS model, TM mode grows and quasi-linear saturation occurs as is explained in the previous paragraph. For B model, the collisional drift wave is saturated at $t = 3000$ with the low amplitude $E_A(n) \simeq 10^{-7}$ ($n > 1$), then at $t \simeq 5000$, TM is saturated with the high amplitude $E_A(n = 1) \simeq 5 \times 10^{-2}$. The behavior in the second phase is similar to that of HS model. The main difference is that for B model, $E_A(n = 0)$ is comparable to $E_A(n = 1)$ in the second saturation phase and the saturation amplitude of $E_A(n = 1)$ is 1 order larger than that of HS model.

Figures (20) and (21) show the time slices of power spectrum of electromagnetic energy in n space for HS and B model, respectively. For HS model, TM grows and the energy is transfered to high n modes. The zonal field ($A_{0,0}$) is mainly generated by the coupling of (2,1) and (-2,-1) modes which contribute to the quasi-linear saturation of TM. For B model, two stages of saturation are clearly observed in the power spectrum. At $t = 3000$, high n modes saturate at the low amplitude

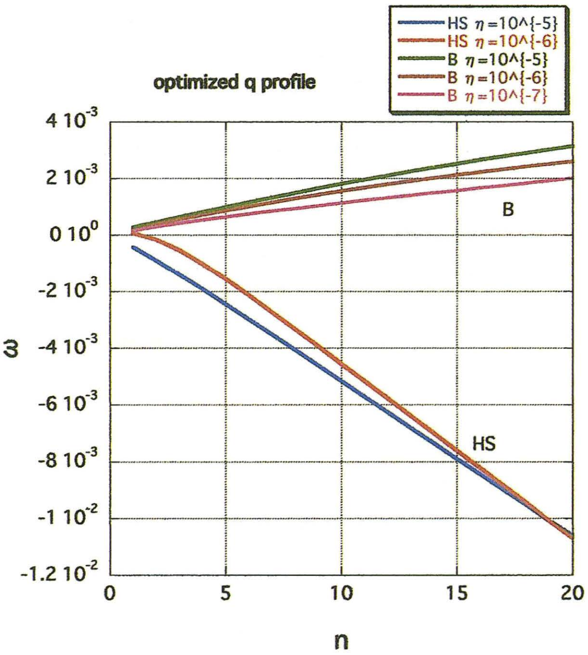

Fig. 15 Dependence of the frequency ω on the toroidal mode number n: The similar tendency is observed as the case with normal q profile.

with $E_A(n) \simeq 10^{-7}$ as is explained in the previous paragraph, while TM is still growing then at $t = 5000$, the quasi-linear saturation occurs and at $t = 20000$, the zonal field saturates. After the quasi-linear saturation, the energy of high n mode decreases gradually while that the zonal field increases until it saturates. The amplitude of zonal field is higher than that of HS model, which is contributed by the high n collisional drift wave components.

Next, we discuss the zonal flow generation.

Figures (22) and (23) show the temporal evolutions of electrostatic energy for the cases with HS model and B model, respectively. The behavior of these evolution is quite similar to those in Figs. (18) and (19). However, the saturation amplitude is very low. For HS model, the zonal flow is the order of $E_F(n = 0) \simeq 10^{-7}$ and for B model, $E_F(n = 0) \simeq 10^{-5}$. This difference comes from the contribution of high n collisional drift wave. However, the zonal flow does not play important role for island saturation. If the turbulence is stronger such as the ballooning type turbulence, then the zonal flow might play a crucial role. It is beyond the scope of this thesis and is left for future work.

Figures (24) and (25) show the time slices of power spectrum of electrostatic energy in n space for HS model and B model, respectively. For HS model, $E_F(n = 1)$ saturates at $t = 6000$, then the zonal flow $E_F(n = 0)$ and high n modes $E_F(n > 1)$ grow gradually until $t = 8000$ and saturate. The saturation amplitude of whole modes is roughly of the order of $10^{-7} \sim 10^{-6}$. For B model, $E_F(n = 1)$ saturates at $t \simeq 4000$. After that, the zonal flow $E_F(n = 0)$ and high n modes $E_F(n > 1)$ saturate at $t = 6000$ and decrease gradually and attain the steady state at $t = 20000$. In this case, the amplitude of $E_F(n = 1)$ is of the order of $\sim 10^{-5}$, while the amplitudes of high n modes $E_F(n > 1)$ are of the order of $10^{-7} \sim 10^{-6}$. We can say that the structure formation in the flow field is really driven by the collisional drift wave.

Figures (26) and (27) show the temporal slices of mode frequencies vs. n for HS model and B model, respectively. The mode frequencies are initially random. For HS model, the phase is adjusted each other at $t = 8000$ where the propagations i. e. , the signs of frequencies are in the ion diamagnetic direction, and gradually decrease. For $t = 30000$, they change the sign and weakly rotate in the electron diamagnetic direction. For B model, the phase adjustment occurs at $t \simeq 5000$. In this case, whole mode frequencies are positive, i. e. , in the ion diamagnetic direction and oscillate; For $5000 < t < 6000$, frequencies decrease to almost zero, then for $6000 < t < 8000$, they start to increase again then they decrease to zero for $8000 < t < 30000$. This behavior might be related with neoclassical damping of flow.

Figures (28) and (29) show the contour plot of helical flux of NTM at $t = 30000$ and the contour plot of kinetic energy of NTM parallel to the magnetic field at $t = 30000$, respectively. The magnetic island is observed. And it is observed that the velocity direction is change at the edge of the magnetic island because the kinetic energy becomes large there.

Finally, we will summarize our numerical results briefly. In our simulation, the neoclassical tearing mode (NTM) is driven by $\Delta' > 0$ and neoclassical viscosity μ_e^{neo}. Our terminology of NTM is different from the conventional one, which indicates the nonlinear instability of tearing mode with $\Delta' < 0$ driven by μ_e^{neo}. B model enables to produce the system where unstable MHD mode and unstable drift wave coexist. Using this model, we investigate the interaction between MHD mode and weak collisional drift wave turbulence. In the growing phase, the acceleration of (2,1) mode is driven by the three wave interaction due to the high n modes, however, the island saturation is dominated by quasi-linear effect. In our case, the island width might be determined by the balance $\Delta'(> 0) + \tilde{\Delta}' + (bootstrap\ current) \simeq 0$. Since the relation $\Delta'(> 0) + \tilde{\Delta}' < 0$ is hold in the saturation phase, the careful experimental measurement of q profile is required to identify NTM is linearly or nonlinearly driven. So far, Δ' is evaluated by the cylindrical model not toroidal model in almost experiments, the decisive conclusion can not be drawn. This point should be resolved in collaboration with experimentalists. This is left for a future work.

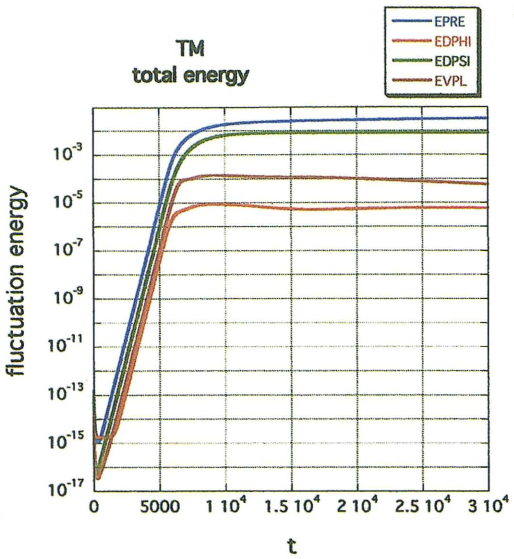

Fig. 16 Temporal evolutions of fluctuation energy for the cases with HS model: The blue curve represents E_p, the green curve E_A, the brown curve $E_{v_\parallel}$ and the orange curve E_F. E_p and E_A are dominant in the total energy. This figure corresponds to the nonlinear simulation of TM. The linear growth and quasi-linear saturation is attained.

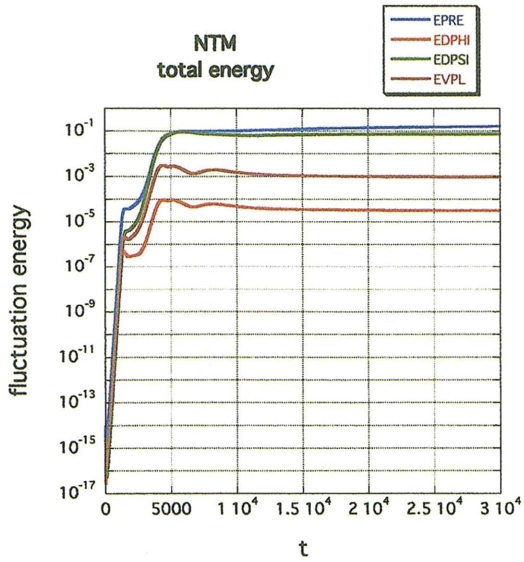

Fig. 17 Temporal evolutions of fluctuation energy for the cases with B model: This figure corresponds to the nonlinear simulation of NTM. Two step saturation is observed. The TM growth is driven by the beat interaction of high n modes so that the linear growth rate of TM plays no role in the growing phase $t \leq 1000$. Then the first saturation is observed at $t \simeq 1000$. In this phase, the high n collisional drift waves are saturated at the low amplitude, and TM continues to grow. At $t \simeq 5000$, the second saturation is observed where TM is saturated quasi-linearly. This time is almost half of that in HS model.

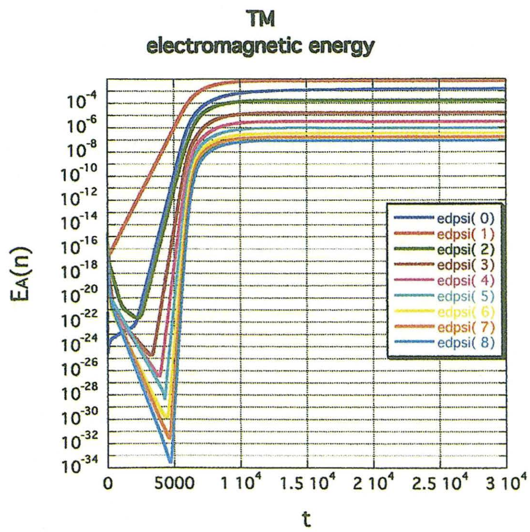

Fig. 18 The temporal evolution of electromagnetic energy of each Fourier mode for the cases with HS model: TM mode grows and quasi-linear saturation occurs as is explained in the previous paragraph.

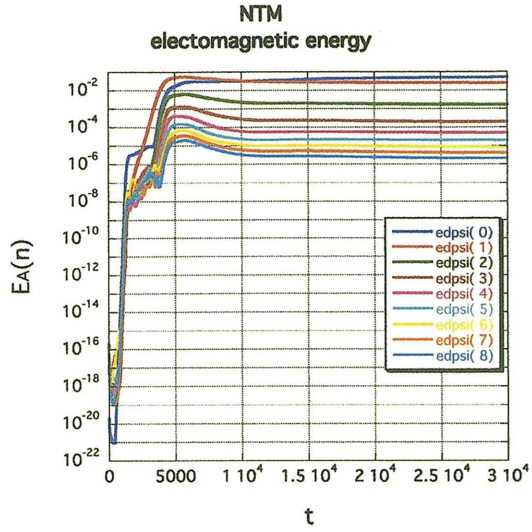

Fig. 19 The temporal evolution of electromagnetic energy of each Fourier mode for the cases with HS model: The collisional drift wave is saturated at $t = 3000$ with the low amplitude $E_A(n) \simeq 10^{-7}$ $(n > 1)$, then at $t \simeq 5000$ TM is saturated with the high amplitude $E_A(n = 1) \simeq 5 \times 10^{-2}$. The behavior in the second phase is similar to that of HS model.

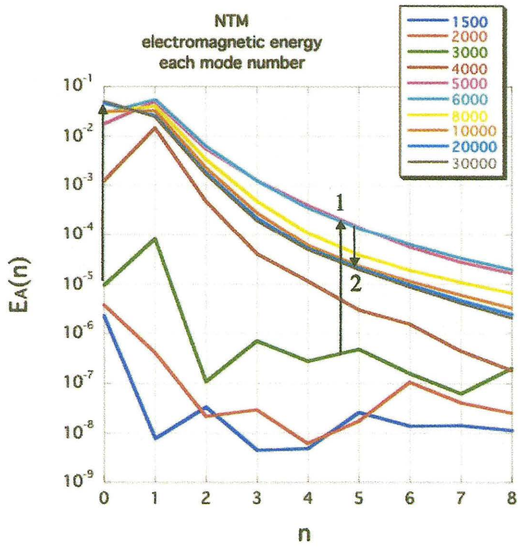

Fig. 21 The time slices of power spectrum of electromagnetic energy in n space for B model: two stages of saturation are clearly observed in the power spectrum. At $t =$ 3000, high n modes saturate at the low amplitude with $E_A(n) \simeq 10^{-7}$ as is explained in the previous paragraph, while TM is still growing then at $t = 5000$, the quasi-linear saturation occurs and at $t = 20000$, the zonal field saturates.

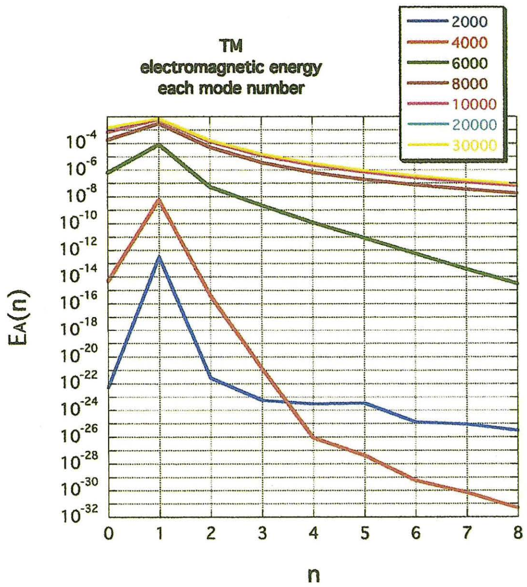

Fig. 20 The time slices of power spectrum of electromagnetic energy in n space for HS model: TM grows and the energy is transfered to high n modes. The zonal field $(A_{0,0})$ is mainly generated by the coupling of (2,1) and (-2,-1) modes which contribute to the quasi-linear saturation of TM.

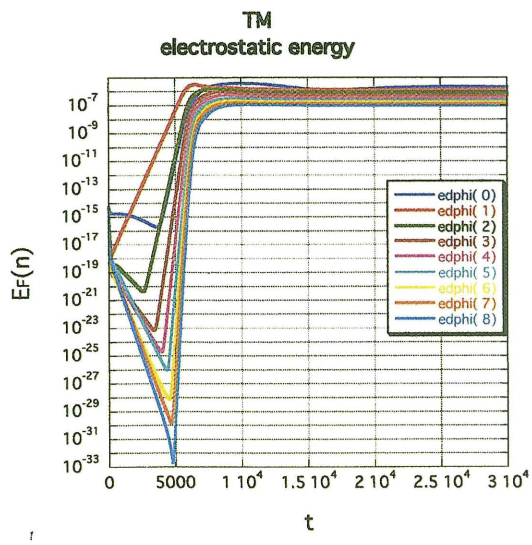

Fig. 22 Temporal evolutions of electrostatic energy for the cases with HS model: The behavior of this evolution is quite similar to that in Figs. (18). However, the saturation amplitude is very low. The zonal flow is the order of $E_F(n = 0) \simeq 10^{-7}$.

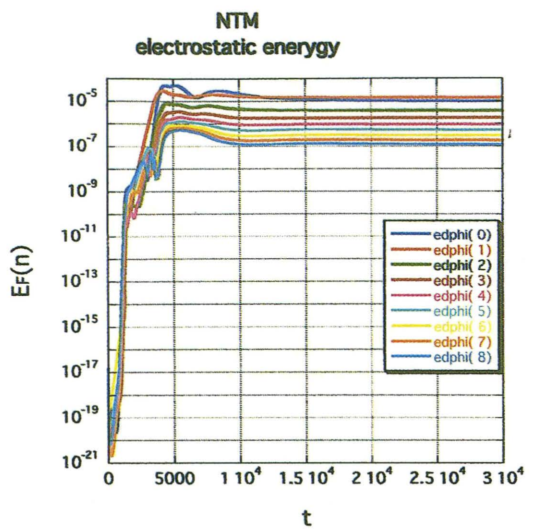

Fig. 23 Temporal evolutions of electrostatic energy for the cases with B model: The behavior of this evolution is quite similar to that in Fig. (19). However, the saturation amplitude is very low. The zonal flow is the order of $E_F(n=0) \simeq 10^{-5}$

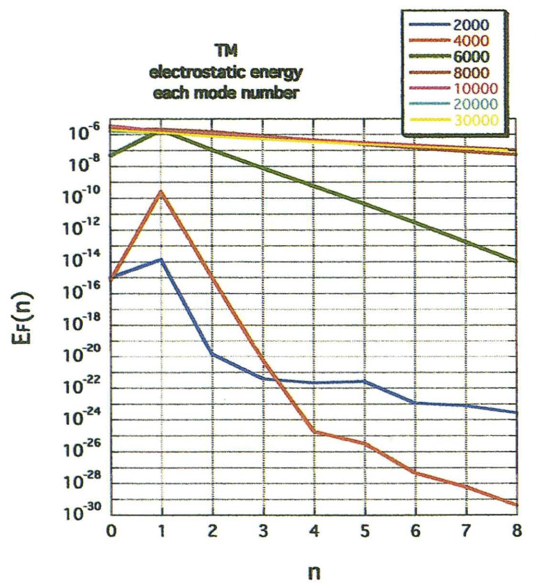

Fig. 24 The time slices of power spectrum of electrostatic energy in n space for HS model: $E_F(n=1)$ saturates at $t=6000$, then the zonal flow $E_F(n=0)$ and high n modes $E_F(n>1)$ grow gradually until $t=8000$ and saturate. The saturation amplitude of whole modes is roughly of the order of $10^{-7} \sim 10^{-6}$.

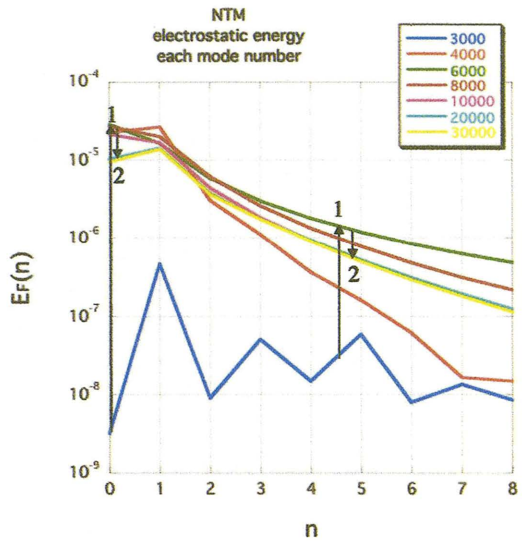

Fig. 25 The time slices of power spectrum of electrostatic energy in n space for B model: $E_F(n=1)$ saturates at $t \simeq 4000$. After that, the zonal flow $E_F(n=0)$ and high n modes $E_F(n>1)$ saturate at $t=6000$ and decrease gradually and attain the steady state at $t=20000$.

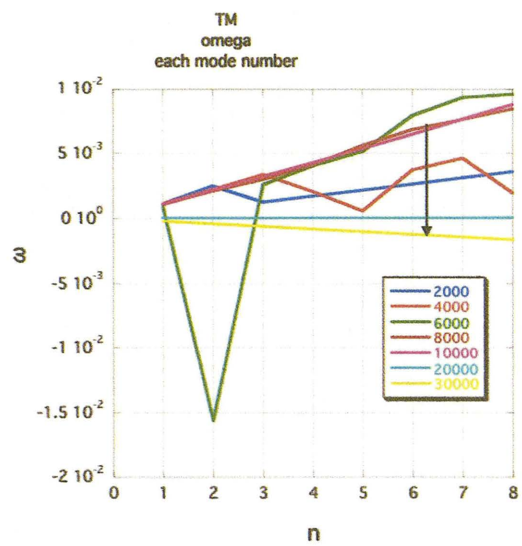

Fig. 26 The temporal slices of mode frequencies vs. n for HS model: The mode frequencies are initially random. For HS model, the phase is adjusted each other at $t=8000$ where the propagations i. e. , the signs of frequencies are in the ion diamagnetic direction, and gradually decrease. For $t=30000$, they change the sign and weakly rotate in the electron diamagnetic direction.

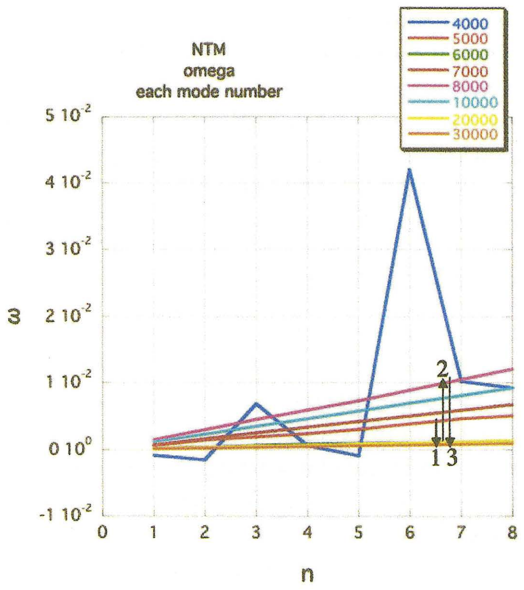

Fig. 27 The temporal slices of mode frequencies vs. n for B model: For B model, the phase adjustment occurs at $t \simeq 5000$. In this case, whole mode frequencies are positive, i. e. , in the ion diamagnetic direction and oscillate; For $5000 < t < 6000$, frequencies decrease to almost zero, then for $6000 < t < 8000$, they start to increase again then they decrease to zero for $8000 < t < 30000$.

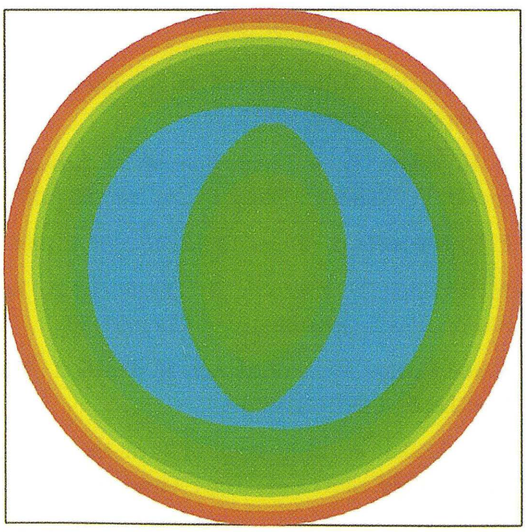

Fig. 28 Contour plot of helical flux of NTM at $t = 30000$: The magnetic island is observed.

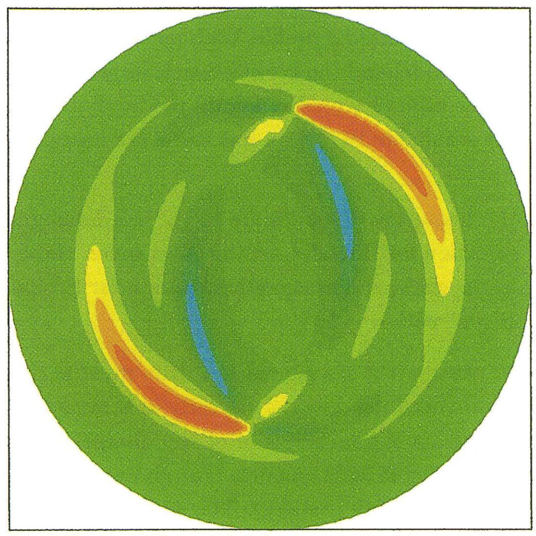

Fig. 29 Contour plot of kinetic energy of NTM parallel to the magnetic field at $t = 30000$: It is observed that the velocity direction is change at the edge of the magnetic island because the kinetic energy becomes large there.

5. Summary

We investigate interaction between tearing mode and collisional drift wave using reduced neoclassical MHD equations. Introducing two types of neoclassical viscosity model, e.g., Hirshman-Sigmar interpolation (HS) formula and banana (B) model, we examine the stability of tearing mode and collisional drift wave in the range of $10^{-7} \leq \eta_{\parallel}^{cl} \leq 10^{-5}$. Also, we investigate the stability of these modes on q profile; the normal q profile with $\Delta' > 0$, and the optimized q profile, where the tearing mode is stable. It is found that

1. in the normal q profile, tearing mode and high n mode are both unstable for B model, on the other hand, only tearing mode is only unstable for HS model,
2. in the optimized q profile, both modes are unstable for B model and the growth rate is larger than that in the normal q profile, for HS model, both modes are stable for $10^{-6} \leq \eta$, but these are unstable for $\eta = 10^{-7}$,
3. the frequency of modes are in the ion diamagnetic direction for B model, on the other hand, these are in the electron diamagnetic direction for HS model except with $\eta = 10^{-7}$.

We observe the collisional ion drift wave is driven by the enhanced neoclassical viscosity in B model. This result suggests the importance of the dissipation form on the stability of MHD modes. The choice of the form changes the stability property. The appropriate form of neoclassical viscosity in the collisionless limit is necessary for realistic applications. It is left for future work.

Next, we perform nonlinear simulations for two cases:

1. HS model with $\eta = 10^{-5}$ and normal q profile (the nonlinear simulation of TM), and
2. B model with $\eta = 10^{-5}$ and normal q profile (the nonlinear simulation of NTM and collisional ion drift waves).

In the case (1), we observe the linear growth of TM and then quasi-linear saturation. On the other hand, in the case (2), we observe two step saturation; in the first phase, high n modes saturate at low amplitude and (2,1) mode continues to grow and in the second phase, (2,1) mode saturates through the quasi-linear effect which is similar to the case (1). It is also found that the growth of TM is accelerated by the nonlinear beat interaction of high n mode so that the linear growth of TM is not observed in the case (2). We also investigate zonal flow generation and structure formation in the flow field. It is concluded that the zonal flow does not play important role for the saturation of magnetic island, although the structure formation in the flow field really occurs due to high n drift waves in the case (2). The frequencies of modes adjust the each phase via the nonlinear effect and oscillatory decrease to zero via the neoclassical damping process. In this research, we did not consider ballooning types turbulence, in which case, the turbulence is more violent so that the zonal flow might play a crucial role for island saturation. It should be investigated near future.

Acknowledgment

It is a great pleasure to thank Professor Sanae -I. Itoh for affording me the opportunity to study plasma physics for fusion research and write this thesis.

I would like to express my special gratitude to Professor Masatoshi Yagi for teaching and guiding me over the two years. Without his patient support and precious advises, this thesis would not have been completed.

I am very grateful to Dr. Masafumi Azumi (Japan Atomic Energy Agency) for his useful comments and suggestions on the manuscript.

Furthermore, I wish to thank Mr. Shinsuke Tokunaga and Mr. Daichi Hamada for their support and useful discussions. I am also indebted to all classmates in Advanced Engineering Science.

Finally, I thank my family for their supports.

This work is partly supported by the Grant-in-Aid for Specially- Promoted Research of MEXT(16002005), by the Grant-in-Aid for Scientific Research of JSPS(16360459) and by the collaboration programs of NIFS and of the Research Institute for Applied Mechanics of Kyushu University.

References

1) H. P. Furth, J. Killeen and M. N. Rosenbulth : Phys Fluids 6, 459 (1963)
2) R. B. White, D. A. Monticello, M. N. Rosenbulth and B. V. Waddell : Phys. Fluids 20, 800 (1977)
3) P. H. Rutherford : Phys. Fluids 16 (1973) 1903
4) A. Isayama, Y. Kamada, T. Ozeki and N. Isei : Plasma Phys. Control.Fusion 41 (1999) 35
5) S. von Goeler, W. Stodiek and N. Sauthoff : Phys. Rev. Lett. 40 (1974) 1201
6) J. D. Callen et. al. : Proc of 11th Int. Conf. on Plasma Phys. and Contr. Nucl. Fusion Res. 2 (1987) 149
7) Smolyakov A I : Plasma Phys. Control. Fusion 35 (1993) 657
8) A. Furuya, M.Yagi and S. -I. Itoh : J. Phys. Soc. Jpn 72 (2003) 313

9) A. Furuya, M. Yagi and S. -I. Itoh : J. Phys. Soc. Jpn 71 (2002) 1261

10) J. D. Callen and Shaing K C : Phys. Fluids 28 (1985) 1845

11) Richard Fitzpatrick : Phys. Plasmas 2 (1995) 825

12) S. -I. Itoh, K. Itoh, H. Zushi and A. Fukuyama : Plasma Phys. Control. Fusion 40 (1998) 879

13) S.P. Hirshman and D. J. Sigmar : Nuclear Fusion 21 (1981) 1079

14) P. Helander D. J. Sigmar : Collisional Transport in Magnetized Plasmas (2002)

15) JET Team (presented by Campbell D J): 1991 Plasma Physics and Controlled Nuclear Fusion Research 1990 vol 1 (Vienna: IAEA) p437

16) J. A. Wesson et. al. : Nuclear fusion 18, 1 (1978)

17) O. J. Kwon, P. H. Diamond and H. Biglari : Phys. Fluids B, 2 (1990) 291